# Generalization of A Kinematic Model of Non-spherical Grains with Application to Hopper Flows

by

Shirin Shiri

B.Sc. with Honors, Sharif University of Technology, Iran, 2017

A Thesis Submitted in Partial Fulfillment of the

Requirements for the Degree of

MASTER OF APPLIED SCIENCE

in the Department of Mechanical Engineering

Generalization of A Kinematic Model of Non-spherical Grains with Application to Hopper Flows

by

Shirin Shiri

B.Sc. with Honors, Sharif University of Technology, Iran, 2017

Supervisory Committee

---

Dr. Ben Nadler, Supervisor

(Department of Mechanical Engineering)

---

Dr. Rustom Bhiladvala, Departmental Member

(Department of Mechanical Engineering)

## ABSTRACT

Granular materials are abundant in nature and industries, and their flow has been subjected to various experimental, analytical and numerical studies over the last decades. The granular flow applications is extended from sorting, packing, and transporting grains and pharmaceutical particles to the study of avalanches and soil erosion. Most of the studies focused on spherical grains. However, most grains in actual applications are geometrically ellipsoidal. Despite being common, the behaviour of the ellipsoidal grains and their response to the flow remain challenging to predict since their ellipsoidal shape brings the effect of the grain orientation to their mechanical response, which has been ignored in most studies. To study the tendency of ellipsoidal grains to align, this work first investigates the performance of a kinematic model that relates the flow to the evolution of the grain alignment. This is done by performing a numerical analysis for discharging ellipsoidal grains in a flat bottom hopper with various opening sizes. After that, two model parameters that can determine the tendency to align and the misalignment of the grains due to collision are generalized according to the shape of the grains and the level of the mutual alignments that is called the ordering factor. These two model parameters should be used along with the model to capture the effect of the grain orientation. The validity of the generalized model is supported by applying it in discharging prolate (rice) and oblate (lentil) grains from a flat bottom hopper and then comparing the outcome with the available experimental results. To reveal the improvement of the generalized model compared to the original model, the differences of the calculated orientational fields are quantified and visualized for the studied grains and conditions. The outcome of this work indicates that the generalized model is in a better agreement with experimental results in capturing the orientational flow of the ellipsoidal grains. This work also advances the capability of the model in capturing the flow type.

# Contents

**Supervisory Committee** **ii**

**Abstract** **iii**

**Contents** **iv**

**List of Tables** **vi**

**List of Figures** **vii**

**Acknowledgements** **xi**

**Dedication** **xii**

**1 Introduction** **1**

1.1 Granular Material Definition . . . . . 2

1.2 Granular Material Modeling . . . . . 4

1.3 Objectives . . . . . 7

1.4 Thesis Structure . . . . . 8

**2 Background Theory** **9**

2.1 The Kinematic Continuum Model to Predict the Orientation and Alignment of Ellipsoidal Grains . . . . . 10

2.2 The Orientation Field Dependency on the Grain Shape in a Hopper Flow . . . . . 16

**3 Model Performance Investigation and Generalization Methodology 20**

3.1 Domain and Equations Discretization . . . . . 21

3.2 Simulation Setup . . . . . 25

3.3 Model Generalization . . . . . 28

**4 Results and Discussions 35**

4.1 Orientation Distribution Visualization Method . . . . . 36

4.2 Model Performance Results and Discussion . . . . . 38

4.2.1 Comparison of the Model Performance and Experiment . . . . 41

4.2.2 Generalized Model Performance Results Comparison with Model and Experiment . . . . . 43

4.2.3 Improvement Quantification . . . . . 47

**5 Conclusion and Future Works 52**

5.1 Summary . . . . . 52

5.2 Future Work . . . . . 54

**Bibliography 56**

# List of Tables

Table 2.1 Properties of the grains used in [22]. . . . . 18

Table 4.1 Values of the generalized model parameters. . . . . 43

Table 4.2 Comparison of the performance of the model and generalized model calculations using the norm of the differences between the orientational domain of the experiment and the model, as well as the generalized model divided by the norm of the orientational domain of the experiment. . . . . 48

Table 4.3 Improvement of the generalized model compared to the model. . 48

# List of Figures

Figure 1.1 An example of three material phases at the same time. Solid, liquid, and gas states of the sand set in a desert. . . . . 2

Figure 1.2 The difference between cohesion and repulsive forces can be seen in (a) and (b), respectively. Cohesion is an attraction between grains (molecules) of the same substance, while repulsive force is a repellent force between two or more grains. Dry granular materials are not affected by cohesion, while they can be affected by inter-grain repulsive forces. . . . . 3

Figure 1.3 Examples of the oriented ellipsoidal grains. (a), (b) and (c) represent rice, capsules, and lentils. The $l$ and $d$ represent the length and diameter of each grain. . . . . 6

Figure 2.1 The length and diameter of the grains are shown with the geometrical parameters named "l" and "d". (a) shows a spherical grain with its length equal to its diameter. While in (b) and (c), in prolate and oblate grains, length is different from the diameter. 11

Figure 2.2 The experimental setup representation including the hopper, the opening, and two X-ray detectors that sit in two different angles to capture the grains orientations and direction of the flow [22]. 17

Figure 3.1 Geometry of the flat bottom hopper employed for the kinematic model simulations. Width, length and height of the hopper are 130mm, 150mm and 300mm, respectively. Two different width sizes for the openings as $W_o = 10, 15$mm are considered in the simulations. . . . . 26

Figure 3.2 Algorithm used to find the best values for $\lambda_a$, $\lambda_b$, $\psi_a$, $\psi_b$ and $\psi_c$. 32

Figure 3.3 Figure of $\lambda(r_g, \zeta)$ taken from curve fitting, using the values of $\lambda$, $r_g$ and $\zeta$ from [21] to show the performance of the proposed model of $\lambda$ with homogeneous data. . . . . 33

Figure 3.4 Figure of $\psi(r_g, \zeta)$ taken from curve fitting, using the values of $\psi$, $r_g$ and $\zeta$ from [21] to show the performance of the proposed model of $\psi$ with homogeneous data. . . . . 33

Figure 4.1 Eigenvalues and Eigenvectors of each grain used to find the angle between ovals and horizontal axis. $\mathbf{a}_1$, $\mathbf{a}_2$ and $\theta$ are the eigenvectors and angle between the larger eigenvector and horizontal line, respectively. . . . . 37

Figure 4.2 Principal angle domain of experimental results of [22]; Rice and Lentil discharges through 10mm and 15mm openings. The color bars provided for all four figures are showing the degree ranges of all the grains within $-90$ to 90 degrees. a) and b) show Rice discharge, c) and d) show Lentil discharge through 10mm and 15mm openings, respectively. . . . . 39

Figure 4.3 Principal angle of model calculations; Rice and Lentil discharges through 10mm and 15mm openings. The color bars provided for all four figures are showing the degree ranges of all the grains within −90 to 90 degrees. a) and b) show Rice discharge, c) and d) show Lentil discharge through 10mm and 15mm openings, respectively. . . . . 42

Figure 4.4 Comparison of the orientational domain of experimental results of [20], model and generalized model calculations; Rice discharges through 10mm and 15mm openings. Blue and red ovals show the experiment, model and generalized model results, respectively. a) and c)Experiment vs. Model results, b) and d)Experiment vs. Generalized model results. . . . . 45

Figure 4.5 Comparison of the orientational domain of experimental results of [20], model and generalized model calculations; Lentil discharges through 10mm and 15mm openings. Blue and red ovals show the experiment, model and generalized model results, respectively. a) and c)Experiment vs. Model results, b) and d)Experiment vs. Generalized model results. . . . . 46

Figure 4.6 Difference percentage of the experiment, model and generalized model results of the orientational domain of Rice discharge through 10mm and 15mm openings. The color bars provided for all four figures are showing the difference ranges between the orientational domains between 0% and 100%. (a) and (c) show model calculations compared to experiment results, (b) and (d) show generalized model calculations compared to experiment results. 49

Figure 4.7 Difference percentage of the experiment, model and generalized model results of the orientational domain of Lentil discharge through 10mm and 15mm openings. The color bars provided for all four figures are showing the difference ranges between the orientational domains between 0% and 100%. (a) and (c) show model calculations compared to experiment results, (b) and (d) show generalized model calculations compared to experiment results. . . . . 50

# ACKNOWLEDGEMENTS

I have received a great deal of support and assistance throughout this dissertation, without whom this work would not have been possible. I would like to express my deepest appreciation to my supervisor, **Dr. Ben Nadler**, whose guidance, support and encouragement have been invaluable throughout this study. Your insightful feedback pushed me to sharpen my thinking and brought my work to a higher level.

I would also like to extend my gratitude to the **supervisory committee members** for their time and effort in evaluating my work.

Finally, I would like to thank my friend, **Bardia Barabadi**, whose consultation and insightful advice was always a precious help to me.

*As you start to walk on the way, the way appears.*

*Rumi*

# DEDICATION

This thesis is dedicated to my beloved parents,

without whom none of my successes would have been possible.

Thank you for your endless love and constant support.

# Chapter 1

# Introduction

This chapter gives a brief description of the granular material and their relevant flows. Moreover, the history of kinematic models and their importance in industry and nature are reviewed in the background and related sections. Furthermore, the main objectives and the contributions of this work, as well as the structure of the thesis are discussed in the subsequent sections of this chapter.

## 1.1 Granular Material Definition

Granular materials are a collection of discrete, macroscopic solid grains. These grains cannot be classified under solid, liquid, or gas formations due to their distinctive characteristics and properties. The material behaviour can switch from solid-like, which is able to support static shear loads, to liquid-like, which can flow in a dense state, to gas-like, in which grains can separate, collide and compress; all three states are shown in Figure (1.1).

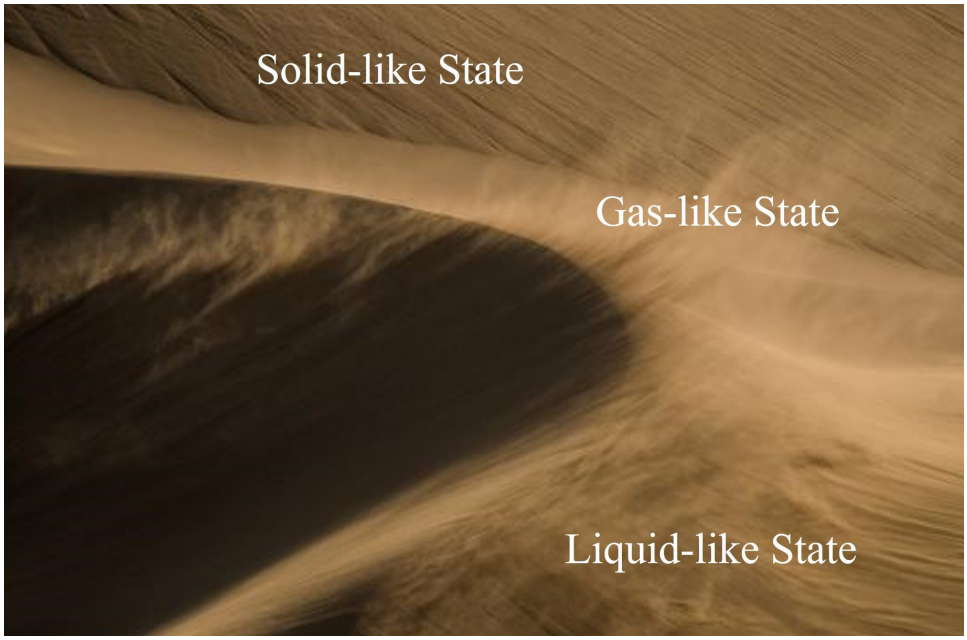


Figure 1.1: An example of three material phases at the same time. Solid, liquid, and gas states of the sand set in a desert.

Granular materials are omnipresent in nature and industry. They are considered the second-most manipulated material in the world, after water [1]. There are plenty of instances where granular materials are found in nature, such as sands, powders, dusts, and gravel. Moreover, industries like agriculture, food processing, pharmaceutics, energy, civil and construction industries deal with these types of materials in their processes every day. The size of a single component of this material can be as

small as one micron or as large as the size of asteroids in the asteroid belts of the Solar System [2, 3]. This broad range of shapes and sizes of grains, along with the distinct and complex flow behaviour and properties of the granular matter, have attracted significant research interest for over fifty years [4, 5].

Granular material with no liquids between their grains is called dry granular material. They are cohesion-less and they carry the repulsive contact forces between their components, as can be seen in Figure (1.2), as if they are not individual pieces but an entirely new material that does not chemically interact [6]. The flow of these grains that happens in their liquid-like phase is called granular flow. Granular flow is quite different from the conventional fluid flow. For instance, granular material grains are not affected by temperature as the atom of each grain is not struggling with the other atoms, so thermal motion fluctuations are negligible in the granular flows [7].

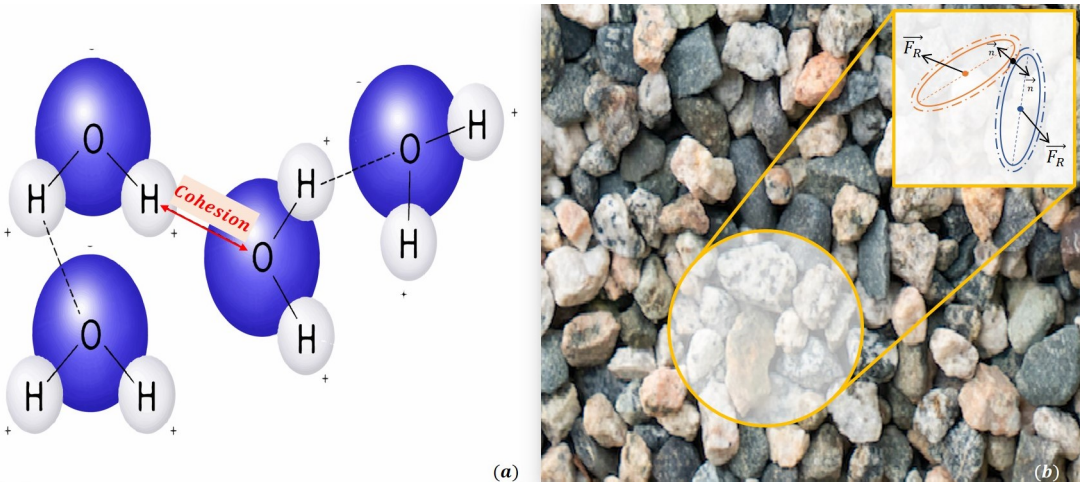


Figure 1.2: The difference between cohesion and repulsive forces can be seen in (a) and (b), respectively. Cohesion is an attraction between grains (molecules) of the same substance, while repulsive force is a repellent force between two or more grains. Dry granular materials are not affected by cohesion, while they can be affected by inter-grain repulsive forces.

Unlike liquids, which can flow and deform continuously under shear forces, granular materials can flow only if certain conditions are satisfied; otherwise, the material

is considered to be jammed, i.e. does not move despite the net force acting on it. Finding out the conditions under which granular media can transform from being a solid jammed material to one that can flow and orient can help control undesirable issues. For example, geotechnical engineering, grains handling and transportation, and mining and milling operations can utilize such information. Moreover, knowing more about these conditions helps to be prepared for natural disasters, and occurrences such as snow or debris avalanches and earthquake-induced soil liquefaction [8]. Therefore, continuum models are required where physical experiments are not feasible due to time, cost and resource limitations to study such complex situations. However, despite the granular material and its applications being common in the world, continuum models have not yet become mature enough to predict the behaviour of non-spherical granular material, during their flow, that can be used universally [9].

## 1.2 Granular Material Modeling

Different experimental and numerical approaches, at different time and length scales, have been developed in the past to explain the granular material flow behaviour and the dependence of mechanical response on the structure. However, formulating a model that can predict the material behaviour during flow can help to minimize the need of having physical experiments or determining massive numerical approximations.

To achieve this goal, continuum approaches are developed to model the granular material on the macroscopic level. The properties of the continuum system are considered continuous in such a way that a piece of material, at any scale, exhibits the same properties as the bulk material. This means that even if the volume of material approaches to zero, still the same properties are recognizable such as same density.

Various theories for different materials and flow regimes have been introduced to develop continuum models in the past. In [10], a constitutive law was proposed for the rate-independent deformation of granular materials in soil mechanics based on either plasticity or shearing theory for quasi-static regimes. On the other hand, collisional rapid flow of granular materials has been modelled in [11] based on the kinetic theory of dense gases. These two approaches have been used to study the transitional regime, which is associated with both collisional and frictional mechanisms [12]. Even though, these models are conducted to study the behaviour of the granular materials during different flow types, they are mostly limited to the spherical grains.

Most of the granular flows consist of non-spherical grains. The significant effect of the shape of the grains on the granular flow was investigated through numerical and experimental research, which have shown that grain shape strongly influences the alignment, orientation, and the mechanical response. In general, non-spherical grains show a more complex behaviour compared to spherical grains [13, 14]. Moreover, their inter-grain and microscopic interactions can happen along their surface area as opposed to the spherical grains which contact each other at a point. Due to the collisional interaction between grains, non-spherical grains form a slight angle with the direction of the flow [15]. Furthermore, the ellipsoidal grains tend to align along their larger aspect with the direction of the flow [16], since the direction of alignment is reflected in the orientation of the ellipses. In [17, 18] it has been observed that an increase in the grain aspect ratio leads to a significant decrease in the flow rate of the grains, in which jamming and clogging can develop more easily compared to the spherical grains [19]. In addition, it was observed in [20] that higher packing densities in non-spherical grains, compared to their spherical counterparts, can occur due to the random packing.

However, most grains carry a degree of asphericity. Available models typically

consider grain sizes, not shape of the grains, and their influences on the orientation and alignment during the flow. Therefore, determining how the shape of the grains affects their orientation and alignment during the flow, through a concise kinematic model, is of the utmost importance in this field.

Nadler et al. [21] proposed a kinematic model that can relate the flow to the grain orientation. This proposed kinematic model is able to predict the average grain orientation and ordering based on the velocity field and shape of the grains. Moreover, this model is capable of capturing the evolution of the grain alignment and tendency of non-spherical grains to align with respect to each other.

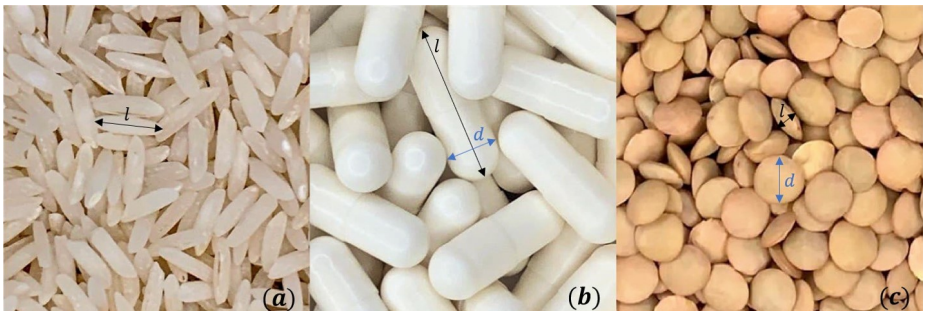


Figure 1.3: Examples of the oriented ellipsoidal grains. (a), (b) and (c) represent rice, capsules, and lentils. The $l$ and $d$ represent the length and diameter of each grain.

Since arbitrary shapes of the grains require a closed surface to facilitate the modelling of the shape, the authors in [21] established an additional extension of grain orientation from the spherical grains that can define any ellipsoidal shape. This new grain orientation characterizes the length of each grain, as can be seen in Figure (1.3).

In [21], the kinematic model was compared with discrete element method (DEM) simulations, which are the numerical methods for computing the motion and effect of a large number of small grains in simple shear flow. Nadler et al. assert that the model showed good agreement with the simulations for steady-state response. Although, the model was examined in homogeneous steady-state, simple shear flow, the performance of the model has not been examined in inhomogeneous flows, where

the orientations and velocities of the grains are variable during the flow. Therefore, the performance of this model needs to be investigated by employing it in actual applications, such as the flow of grains in a hopper, to consider the model accuracy in inhomogeneous flows where the grains have various orientations in different points.

## 1.3 Objectives

This work aims to simulate and compare the kinematic model presented in [21] with an actual application of hopper discharging, in a flat bottom hopper filled with ellipsoidal grains. Furthermore, the other goal of this work is to improve and generalize this kinematic model for non-spherical grains to better predict the orientation and the alignment of the grains during the flow. The main contributions of this work are summarized as:

- The performance of the kinematic model available in [21] is investigated by means of MATLAB, in discharging flow of a flat bottom hopper filled with ellipsoidal grains ranging from oblate (lentil) to prolate (rice). Also, the system of nonlinear equations of the continuum model are solved numerically. Finally the simulation results are visualized to show the model performance and capabilities.

- The model parameters in the kinematic model are generalized to provide a better prediction of the orientation of the grains by extending the model parameters based on the mutual alignment of the grains.

- The performance of the generalized kinematic model is investigated and compared against the discharging granular material flow in a flat bottom hopper to validate the performance of the proposed model.

- The error between available experimental results, model and generalized model predictions are calculated and local errors visually sketched to show the improvement.

## 1.4 Thesis Structure

The present work includes four chapters in addition to the current chapter. The content of each chapter are as follows:

**Chapter 2** demonstrates the theories required to use experiment [22] as the baseline for simulating the model available in [21]. It also includes the kinematic material, model discretization and setup required for simulating and numerically solving the model and generalized model.

**Chapter 3** gives the details of the computational analysis and assumptions required for simulation. Moreover, it presents the model generalization method, parameter formulation, verification and implementation in the hopper discharge.

**Chapter 4** presents the model and generalized model results. It also includes the comparisons of the model and generalized model against the experimental results.

**Chapter 5** contains a summary of the claims and results of this work. Finally, it enumerates avenues of future work for further development of the concept and its applications.

# Chapter 2

# Background Theory

This chapter introduces the continuum model that was developed in [21]. A detailed definition of the model components and its results, compared to the DEM simulations that took place in [21], are addressed in this chapter. The experimental results available in [22] are introduced in the subsequent section. This experiment is used as the baseline for investigating the performance of the model in predicting the orientational flow of the ellipsoidal grains in an inhomogeneous flow.

## 2.1 The Kinematic Continuum Model to Predict the Orientation and Alignment of Ellipsoidal Grains

As discussed earlier, most of the current continuum models in granular flows are designed to be used for spherical grains. However, non-spherical grains show more complex mechanical behaviours than spherical due to their ability to orient and align with respect to each other and the flow. Furthermore, the initial orientation of the grains and orientational evolution over time have a significant effect on the mechanical response of the grains. Therefore, the kinematic continuum model in [21] was developed based on the velocity field and shape of the grains to predict the evolution of the grains' orientation and alignment during the flow. In [21], a representation of the shape of ellipsoidal grains was introduced to define the orientation of the grains. Afterwards, the kinematic model was proposed using shape of the grains. Subsequently, two model parameters which are functions of the grain shape, were determined. The kinematic continuum model was compared with DEM simulations in [21] in simple shear and showed a good agreement with DEM simulations in homogeneous steady state, but not in inhomogeneous flow.

Nadler et al. in [21] defined each individual non-spherical grain and its orientation by using the length of the grain, diameter and a unit vector labeled as $\mathbf{k}$. The unit vector is considered to be along the symmetry axis and defines the orientation of each grain, shown in Figure (2.1). Accordingly, a symmetric probability density function as $f(\mathbf{k})$, and $f(+\mathbf{k}) = f(-\mathbf{k}) \geq 0$, is considered to represent the statistical orientation of the grains at a given point in space and time with

$$\oint_{S^2} f(\mathbf{k})\, da = 1\,, \tag{2.1}$$

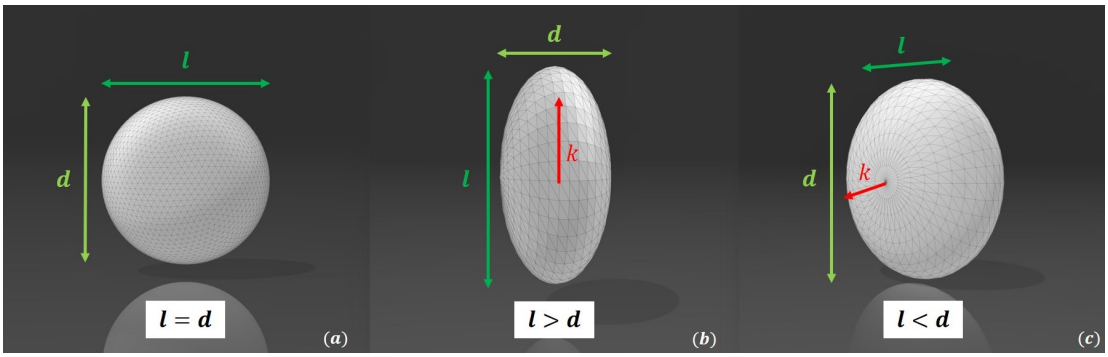


Figure 2.1: The length and diameter of the grains are shown with the geometrical parameters named "l" and "d". (a) shows a spherical grain with its length equal to its diameter. While in (b) and (c), in prolate and oblate grains, length is different from the diameter.

that shows the surface integral of the probability density function, where $S^2$ stands for the unit sphere. This unit sphere covers all the possible orientation of unit vector $\mathbf{k}$. Therefore, the some of posibilities of the orientation of $\mathbf{k}$ over the sphere is equal to one. The second order tensorial moment of $f(\mathbf{k})$ can effectively define the grain orientation distribution of the grains

$$\mathbf{A} = \oint_{S^2} f(\mathbf{k})\, \mathbf{k} \otimes \mathbf{k}\, da\,. \tag{2.2}$$

The orientational tensor $\mathbf{A}$, is considered as a positive semi-definite or non-negative-definite tensor, since $(\mathbf{x}\cdot\mathbf{A}\mathbf{x}) \geq 0$, where $\mathbf{x}$ is any real vector. This is then reorganized to $\mathbf{x} \cdot \big( \oint_{S^2} f(\mathbf{k})\, \mathbf{k} \otimes \mathbf{k}\, da\big)\mathbf{x}$. Now, the $\mathbf{x}$ can be dragged into the integral, considering the fact that it is not a function of $\mathbf{k}$

$$\oint_{S^2} f(\mathbf{k})\mathbf{x} \cdot (\mathbf{k} \otimes \mathbf{k})\, \mathbf{x}\, da = \oint_{S^2} f(\mathbf{k})\mathbf{x} \cdot (\mathbf{k} \cdot \mathbf{x})\, \mathbf{k}\, da = \oint_{S^2} f(\mathbf{k})(\mathbf{k} \cdot \mathbf{x})^2\, da\,. \tag{2.3}$$

Since $f(\mathbf{k}) \geq 0$ by definition, and $(\mathbf{k}\cdot\mathbf{x})^2 \geq 0$ is always non-negative, hence $(\mathbf{x}\cdot\mathbf{A}\mathbf{x}) \geq 0$ which shows that $\mathbf{A}$ is a positive semi-definite tensor. Also, since the tensor product follows the property of $(\mathbf{e} \otimes \mathbf{g})^T = \mathbf{e} \otimes \mathbf{g}$, it can be concluded that $\mathbf{A}$ is symmetric,

by taking the transpose of (2.2)

$$\mathbf{A}^T = (\oint_{S^2} f(\mathbf{k})\,\mathbf{k}\otimes\mathbf{k}\,da)^T = \oint_{S^2} f(\mathbf{k})\,\mathbf{k}\otimes\mathbf{k}\,da = \mathbf{A}\,. \tag{2.4}$$

Using the symmetry property of $\mathbf{A}$, the spectral representation can be expressed as

$$\mathbf{A} = \sum_{i=1}^{3} \alpha_i(\mathbf{a}_i \otimes \mathbf{a}_i)\,, \tag{2.5}$$

where $\alpha_i$ are the eigenvalues of $\mathbf{A}$, with $0 \leq \alpha_i \leq 1$ and $\alpha_1 + \alpha_2 + \alpha_3 = 1$. Also, $\mathbf{a}_i$ are the associated eigenvectors. Since $\mathbf{A}$ is a symmetric tensor, the eigenvalues are real, and the corresponding eigenvectors are mutually orthogonal.

For developing a model that can predict the evolution of the orientational tensor based on the velocity field, the velocity gradient $\mathbf{L}$ is defined as

$$\mathbf{L} = \mathrm{grad}(\mathbf{v})\,, \tag{2.6}$$

where $\mathbf{v}$ is the velocity field of the grains. The velocity gradient (2.6), can be decomposed to the symmmetrical part $\mathbf{D}$, and the antisymmetrical part $\mathbf{W}$ as $\mathbf{L} = \mathbf{D} + \mathbf{W}$. Where $\mathbf{D}$ is the rate of deformation, and $\mathbf{W}$ is the vorticity

$$\mathbf{D} = \frac{1}{2}\big(\mathbf{L} + \mathbf{L}^T\big) = \mathbf{D}^T\,, \quad \mathbf{W} = \frac{1}{2}\big(\mathbf{L} - \mathbf{L}^T\big) = -\mathbf{W}^T\,. \tag{2.7}$$

The rate of change of the orientation tensor $\mathbf{A}$ can be obtained by taking the material time derivative of (2.2) as

$$\dot{\mathbf{A}} = \frac{d}{dt}\oint_{S^2} f(\mathbf{k})\mathbf{k}\otimes\mathbf{k}\,da\,, \tag{2.8}$$

where $\dot{\mathbf{A}}$ is the material time derivative of $\mathbf{A}$. Since the integral domain is not

changing with time, the differentiation operator can be taken into the integral domain, and the equation is reorganized as

$$\dot{\mathbf{A}} = \oint_{S^2} \left( \dot{\overline{f(\mathbf{k})\, da}}\, \mathbf{k} \otimes \mathbf{k} + f(\mathbf{k})\, \dot{\overline{\mathbf{k} \otimes \mathbf{k}}}\, da \right). \tag{2.9}$$

Since, $\mathbf{k}da$ is constant, the first term of the (2.9) vanishes and simplifies as

$$\dot{\mathbf{A}} = \oint_{S^2} f(\mathbf{k})(\dot{\mathbf{k}} \otimes \mathbf{k} + \mathbf{k} \otimes \dot{\mathbf{k}})\, da\,, \tag{2.10}$$

where $\dot{\mathbf{k}}$ is the material time derivative of $\mathbf{k}$, and is defined as a line element travelling with the flow as

$$\dot{\mathbf{k}} = \mathbf{W}\mathbf{k} + \lambda(\mathbf{D} - (\mathbf{k} \cdot \mathbf{D}\mathbf{k})\mathbf{k}\,, \tag{2.11}$$

where the parameter $\lambda$ shows the tendency of the grains to align with the rate of deformation, $\mathbf{D}$. The flow evolution law with two material parameters is presented as

$$\dot{\mathbf{A}} = \mathbf{W}\mathbf{A} - \mathbf{A}\mathbf{W} + \lambda[\mathbf{D}\mathbf{A} + \mathbf{A}\mathbf{D} - 2(\mathbf{A} \cdot \mathbf{D})\mathbf{A}] - \psi \left\| \mathbf{D}' \right\| (\mathbf{A} - \mathbf{I}/3)\,, \tag{2.12}$$

where $\mathbf{I}$ is the identity tensor. Also, the $-2(\mathbf{A} \cdot \mathbf{D})\mathbf{A}$ guarantees that the model is traceless. This term shows that grains stretch as they orient and deform during the flow. Furthermore, the $\left\| \mathbf{D}' \right\| (\mathbf{A} - \mathbf{I}/3)$ models the collision between grains which leads to misalignments of the grains. Also, $\mathbf{D}'$ is the deviatoric part of the rate of deformation expressed as

$$\mathbf{D}' = \mathbf{D} - \frac{1}{3} \operatorname{trace}(\mathbf{D})\mathbf{I}\,, \tag{2.13}$$

where $\left\| \mathbf{D}' \right\|$ is the magnitude of $\mathbf{D}'$ and defined as $\left\| \mathbf{D}' \right\| = \sqrt{\mathbf{D}' \cdot \mathbf{D}'}$.

The model parameters, $\lambda$ and $\psi$, characterize the tendency of alignment of the grains and relaxation toward isotropic distribution, respectively. For simplicity, these

two parameters in [21] are taken to be a function of the shape ratio $r_g$

$$r_g = \frac{l-d}{l+d}\,, \tag{2.14}$$

where $l$ and $d$ are the geometrical length and width of the grains and are shown in Figures (1.3) and (2.1). This shape ratio can take values between $-1$ to 1, where $r_g = 0$ characterizes the spherical grains. Also, $r_g$ is positive and increasing for prolate grains, while it is negative and decreasing for oblate grains.

The model parameter $\lambda$ can be varied from $-1$ to 1 according to the grain shape. The $\lambda = 0$ defines the spherical grains since the rotation due to collision does not change the orientation of the spherical grains. The parameter $|\lambda|$ increases as grains become more ellipsoidal, in such a way that by $|\lambda| \to 1$ one of the grain dimensions diminishes. Since ellipsoidal grains tend to align with respect to their larger dimension with the flow direction, $\lambda$ is positive for prolate grains and negative for the oblate grains. In addition, the material parameter $\psi$ is explained as the measure of misalignment due to grain collisions during the flow. Also, it is assumed to be proportional to the shear rate $\left\|\mathbf{D}'\right\|$. Since the tendency of the grains to align is assumed to be toward random distribution, $\psi$ is recognized as a non-negative parameter. Moreover, $\psi$ is expected to be decreasing for more ellipsoidal grains since it is harder to rotate more ellipsoidal grains. The ellipsoidal grains can collide and lock into each other hence the effect of the rotation due to collision should be less effective on the orientation.

The performance of this kinematic model was examined by using DEM simulations in a three-dimensional configuration in [21]. Using simple shear simulation, the model parameters were determined by comparing the orientational tensor in the steady state obtained by the model and the DEM simulations. Two relationships that agree with

the numerical measurements were obtained by curve fitting as

$$\lambda(r_g) = (2/\pi)\tan^{-1}(5.5r_g), \qquad \psi(r_g) = 0.85\exp(-4r_g^2)\,. \tag{2.15}$$

The curve fittings were based on the data in the range of $r_g \in [-0.6, -0.2]$ and $r_g \in [0.2, 0.7]$. Therefore, the proposed $\lambda$ and $\psi$ might not be accurate in smaller or larger $\left|r_g\right|$ values.

In [21] the kinematic continuum model establishes a good agreement with DEM simulations in simple shear flow. The results of [21] show that model well captures the orientation of the ellipsoidal grains in the simple shear. In the simple shear flow application in [21], the grains were sheared until they reached a homogeneous steady state, where all the grains exhibited the same orientations and velocities in each locations of the medium. Although, the model seemed to work very well for the homogeneous flow, the performance of the model needs to be investigated in the flows with inhomogeneous characteristics, where the grains exhibit variable orientations and velocities during the flow.

To investigate the performance of the kinematic model available in [21] and introduced in the current section, an experimental methodology capable of capturing the flow behaviour, properties, and velocity field of the ellipsoidal grains in an actual application such as silo or hopper discharging is required. The following section will introduce an experimental method that can effectively measure the velocities and orientations of the grains. The experiment that will be introduced in the following section is used as the baseline of this work.

## 2.2 The Orientation Field Dependency on the Grain Shape in a Hopper Flow

Granular material flowing through bottlenecks, such as the openings of silos, have long been a matter of interest for granulate studies. Despite a large number of experimental and theoretical studies of silo problems, silo failures frequently happen. Silo failures mainly occur at the discharge openings, which usually include irreparable damages to the entire silo. The silo discharge failures can be categorized as the frequent arch formation which is the arrangement of the grains at the orifice in which block the flow [23, 24] by jamming or clogging, also arch breaking that is associated with releasing energy[25, 26]. The aforementioned phenomena are among the important features that should be detected and solved to prevent the silo discharge failures.

Most of the discharge failures that happen in silos are caused by the orientational flows of the non-spherical grains, hence studying these flows can help to minimize these types of problems. Non-invasive means are needed to observe and capture the impact of the shapes of the grains on the flow. Therefore, some experimental studies have been conducted that propose tracking techniques to find the flow deformations, such as magnetic resonance imaging (MRI) [27, 28] and X-ray computed tomography (X-ray CT) [29, 30]. According to the studies, it can be said that X-ray CT is the most frequently used technique. However, this technique is restricted to discontinuities since it requires several incremental loading steps for proper radiographic scanning around a sample. These methods are not capable of detecting flow behaviour continuously, hence time delay is in their nature. To overcome these limits, Guillard et al. in [22] proposed a new experimental technique using dynamic X-ray radiography to predict the orientation of the grains during the flow distribution for the flow inside a hopper. The X-ray radiography method is typically used for taking

stationary samples, so it is not associated with any time delay. The velocity field of the granular flow was studied in [22], by taking images through a transparent hopper and using standard image analysis tools for granular material, including grain image velocimetry (PIV) [31] and fourier transformations [32]. In [22] a rectangular flat bottom hopper filled with either spherical or non-spherical grains were used to detect grain velocity and orientation changes during the flow. The hopper dimensions were considered as $H = 300$mm, $W = 150$mm, and $L = 130$mm. To allow the grains flow, a horizontal opening door at the bottom of the hopper was considered with three various widths as $D = 10$mm, 12mm or 15mm. To identify the direction of the flow and the orientation of the grains, two X-ray sources were set up, as can be seen in Figure (2.2). They provided two-dimensional orientational fields from each detector in each direction.

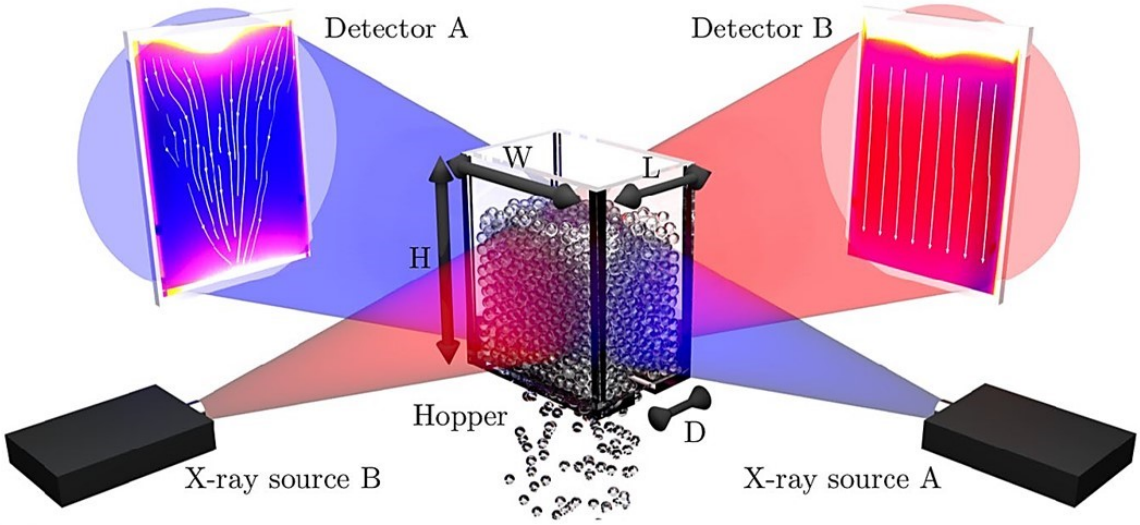


Figure 2.2: The experimental setup representation including the hopper, the opening, and two X-ray detectors that sit in two different angles to capture the grains orientations and direction of the flow [22].

The process of capturing the granular material flow through the hopper was reported in [22] as following. Once discharge started from the bottom opening, after a temporary transient flow, grains vacated the silo at a constant rate as if they were

in steady state. At that time, the radiation of the X-ray Radiography system passed through the hopper walls and captured the granular medium flow. The X-ray sources were arranged to provide the rays perpendicular to the velocities of the grains, shown in Figure (2.2). The configuration of the detector A in the Figure (2.2) contained the inhomogeneous characteristics of the flow since the velocities and the orientations of the grains were different in each location. The configuration of the detector B contained the homogeneous results where velocities of the grains were considered the same in each location. However, the velocities of the grains for both configurations were not constant near the openings in the middle.

| **Material** | **Minor Axis (mm)** | **Major Axis (mm)** |
|---|---|---|
| Jasmine rice | 1.5 | 6.7 |
| Red lentils | 1.6 | 4.5 |
| 3mm glass beads | 2.9 | 3.1 |
| 1mm glass beads | 1.1 | 1.2 |

Table 2.1: Properties of the grains used in [22].

To examine dynamic X-ray radiography method, authors in [22] employed different grains, indicated in Table (2.1), along with three openings for the hopper. Both the funnelling flow in which the grains first vacate the hopper from the middle, and bulk flow in which the grains move down the hopper as a column were observed during the experiments, depending on the grains type and the opening size. The funnelling has been detected to be stronger for smaller outlets and for the ellipsoidal grains. In the presence of the funnelling flow, velocity field happened to be not constant and oscillates over time.

In [22] it was shown that near the opening, the grains reorient toward the center of the channel while they flow down the hopper. It was represented that glass beads which are considered as the spherical grains do not show any ordering during the flow since they do not have any elongated aspect. While jasmine rice and lentils reorient with the flow. The orientation was happened at farther upstream for the smaller

opening compared to the larger one. The orientation alignment was seen when the grains reach the opening, but, the alignment was not parallel to the flow, and grains aligned with respect to each other in a degree with the flow.

It was reported and shown that the experimental results available in [22] showed a good agreement with the actual observations and the previous works. Therefore, the velocity fields and the positions of the grains in the hopper and the setup required for solving the kinematic model of [21] are taken from this experiment. Also, the results of this experiment are visualized and used as the baseline for investigating the performance of the model and showing the improvement of the generalized model.

# Chapter 3

# Model Performance Investigation and Generalization Methodology

In this chapter, the kinematic model of [21] and introduced in chapter (2) is numerically solved using [22], to investigate its performance in hopper flow discharging. The model discretization and all the assumptions made to simulate this kinematic model in a hopper are addressed. Also, the numerical method that was employed to solve this system of nonlinear equations is explained. Then, the ordering parameter, which is a measure of the level of mutual alignment of the grains is introduced to extend the performance of the model parameters. Finally, a linear dependency of the ordering coefficient to the model parameters is proposed to develop the performance of the model.

## 3.1 Domain and Equations Discretization

The continuum kinematic model proposed in [21] is a nonlinear equation and requires the use of a numerical method to solve. In such complex problems, which are nonlinear, discretization can be employed to transform the initially continuous problem into a discrete problem. Therefore, an implicit finite difference approximation is used to solve the kinematic model in [21] numerically.

The velocity field of the flow in three-dimensional space is

$$\mathbf{v} = u\,\hat{\mathbf{i}} + v\,\hat{\mathbf{j}} + w\,\hat{\mathbf{k}}\,, \tag{3.1}$$

where $u$, $v$, and $w$ are velocity components, that lay in $x$, $y$, and $z$ directions, respectively. The $y$ direction is pointing downward perpendicular to the $xz$ plane. Since the governing equation, $\dot{\mathbf{A}}$ in (2.12), is a material time derivative, the derivatives are calculated with respect to time and velocity field

$$\dot{\mathbf{A}} = \frac{\partial \mathbf{A}}{\partial t} + \mathbf{v}\cdot(\operatorname{grad}\mathbf{A}) = \frac{\partial \mathbf{A}}{\partial t} + u\,\frac{\partial \mathbf{A}}{\partial x} + v\,\frac{\partial \mathbf{A}}{\partial y} + w\,\frac{\partial \mathbf{A}}{\partial z}\,, \tag{3.2}$$

where $(\operatorname{grad}\mathbf{A})$ is the gradient of $\mathbf{A}$ with respect to the position. The model is solved in the steady state in the $xy$ plane, hence the time derivative and the velocity in the $z$ direction vanish. Therefore, (3.2) is simplified to

$$\dot{\mathbf{A}} = u\,\frac{\partial \mathbf{A}}{\partial x} + v\,\frac{\partial \mathbf{A}}{\partial y}\,. \tag{3.3}$$

Substituting (3.3) in the equation (2.12) yields

$$u\,\frac{\partial \mathbf{A}}{\partial x} + v\,\frac{\partial \mathbf{A}}{\partial y} = \mathbf{W}\mathbf{A} - \mathbf{A}\mathbf{W} + \lambda[\mathbf{D}\mathbf{A} + \mathbf{A}\mathbf{D} - 2(\mathbf{A}\cdot\mathbf{D})\mathbf{A}] - \psi\left\|\mathbf{D}'\right\|(\mathbf{A} - \mathbf{I}/3)\,. \tag{3.4}$$

The $\partial\mathbf{A}/\partial x$ is the change of $\mathbf{A}$ with respect to the horizontal direction, and $\partial\mathbf{A}/\partial y$ is the change of $\mathbf{A}$ with respect to the vertical direction. Since this model is solved in a hopper, the orientation of the grains downward in $y$ direction contains the evolution of the flow in the height of the hopper. Therefore, to find the rate of evolution of the grains while they flow down the hopper, equation (3.4) is reorganized as

$$\frac{\partial\mathbf{A}}{\partial y} = \left(\mathbf{WA}-\mathbf{AW}+\lambda[\mathbf{DA}+\mathbf{AD}-2(\mathbf{A}\cdot\mathbf{D})\mathbf{A}]-\psi\left\|\mathbf{D}'\right\|(\mathbf{A}-\mathbf{I}/3)-u\,\frac{\partial\mathbf{A}}{\partial x}\right)v^{-1}\,. \quad (3.5)$$

This nonlinear equation is discretized to be solved numerically for $\partial\mathbf{A}/\partial y$

$$\begin{aligned}\frac{\partial\mathbf{A}}{\partial y}\Big|_{i,j} =&\Big(\mathbf{W}_{i,j}\mathbf{A}_{i,j}-\mathbf{A}_{i,j}\mathbf{W}_{i,j}+\lambda[\mathbf{D}_{i,j}\mathbf{A}_{i,j}+\mathbf{A}_{i,j}\mathbf{D}_{i,j}-2(\mathbf{A}_{i,j}\cdot\mathbf{D}_{i,j})\mathbf{A}_{i,j}]\\ &-\psi\left\|\mathbf{D}'_{i,j}\right\|(\mathbf{A}_{i,j}-\mathbf{I}/3)-u_{i,j}\frac{\partial\mathbf{A}}{\partial x}\Big|_{i,j}\Big)v_{i,j}^{-1}\,,\end{aligned} \quad (3.6)$$

where $i$ and $j$ parametrize the $y$ and $x$ dimensions of the domain, where $j$ and $i$ increase toward the right side and down side, respectively. This equation has to be solved vertically in a forwarding order from the top of the hopper to the bottom. This means that, the spatial derivative is approximated by the forward difference approximation for the first-order derivatives from finite difference formulation as

$$\frac{\partial\mathbf{A}}{\partial y}\Big|_{i,j} = \frac{\mathbf{A}_{i+1,j}-\mathbf{A}_{i,j}}{\Delta\, y}\,, \quad (3.7)$$

where $\mathbf{A}_{i,j}$ is the orientational tensor for the current position and $\mathbf{A}_{i+1,j}$ predict the orientational tensor for the next vertical position. Also, $\Delta y$ is the distance between the current and next position of the orientational tensors. By substituting (3.7) into

(3.6) equation, the governing equation is altered to

$$\begin{aligned}\mathbf{A}_{i+1,j} =& \Big( \mathbf{W}_{i,j}\mathbf{A}_{i,j} - \mathbf{A}_{i,j}\mathbf{W}_{i,j} + \lambda[\mathbf{D}_{i,j}\mathbf{A}_{i,j} + \mathbf{A}_{i,j}\mathbf{D}_{i,j} - 2(\mathbf{A}_{i,j}\cdot\mathbf{D}_{i,j})\mathbf{A}_{i,j}] \\ & - \psi\left\|\mathbf{D}'_{i,j}\right\|(\mathbf{A}_{i,j} - \mathbf{I}/3) - u_{i,j}\frac{\partial \mathbf{A}}{\partial x}\Big|_{i,j}\Big)\frac{\Delta y}{v_{i,j}} + \mathbf{A}_{i,j}\,.\end{aligned} \tag{3.8}$$

According to (3.8), forward steps are required to solve this problem numerically. This equation for the first step takes the velocity field and the orientation of the first layer of the grains as the starting point. Next, it calculates the orientation field at the downward layer of the flow. For this purpose, explicit and implicit methods are two approaches that can be used for solving this problem numerically. The explicit method calculates the state of the system using the current step, while the implicit method solves the problem using both the current state and the later step. If the orientation tensors in the right hand side of the equation are converted to the current state of the system by indexing as $\mathbf{A}_{i,j}$, the system of equations is solved explicitly to find the $\mathbf{A}_{i+1,j}$, such as (3.8) equation. On the other hand, if the orientation tensors on the right hand side are indexed with the next steps as $\mathbf{A}_{i+1,j}$, the system of equations is solved implicitly using both $\mathbf{A}_{i,j}$ and $\mathbf{A}_{i+1,j}$ to find the orientational tensors for the next layer of flow. Although the implicit method requires extra computational power, it gives more stable results than the explicit method. Therefore, the implicit method is used here to discretize (3.5) as

$$\begin{aligned}\mathbf{A}_{i+1,j} = \Big( & \mathbf{W}_{i+1,j}\mathbf{A}_{i+1,j} - \mathbf{A}_{i+1,j}\mathbf{W}_{i+1,j} + \lambda[\mathbf{D}_{i+1,j}\mathbf{A}_{i+1,j} + \mathbf{A}_{i+1,j}\mathbf{D}_{i+1,j} \\ & - 2(\mathbf{A}_{i+1,j}\cdot\mathbf{D}_{i+1,j})\mathbf{A}_{i+1,j}] - \psi\left\|\mathbf{D}'_{i+1,j}\right\|(\mathbf{A}_{i+1,j} - \mathbf{I}/3) \\ & - u_{i+1,j}\frac{\partial \mathbf{A}}{\partial x}\Big|_{i+1,j}\Big)\frac{\Delta y}{v_{i+1,j}} + \mathbf{A}_{i,j}\,,\end{aligned} \tag{3.9}$$

where $(i, j)$ and $(i + 1, j)$ show the current and next states, respectively.

To solve the problem and find the orientation tensor of the grains at each point, central differencing needs the next and previous tensors to approximate the derivative of the current point. Therefore, central differencing is not capable of solving the model for the positions at the boundaries of the hopper. Thus, central, forward and backward (one-sided) second-order accuracy of the finite difference formulations are used to approximate the evolution of the grains horizontally in the bulk flow and both boundaries. The discrete approximation of $(\partial \mathbf{A}/\partial x)\Big|_{i+1,j}$ for bulk flow in the middle and boundaries of the hopper are calculated by equations (3.10), (3.11) and (3.12) as

$$\frac{\partial \mathbf{A}}{\partial x}\Big|_{i,j} = \frac{\mathbf{A}_{i,j+1} - \mathbf{A}_{i,j-1}}{2\Delta y}\,, \tag{3.10}$$

$$\frac{\partial \mathbf{A}}{\partial x}\Big|_{i,j} = \frac{-3\mathbf{A}_{i,j} - 4\mathbf{A}_{i,j+1} + \mathbf{A}_{i,j+2}}{2\Delta y}\,, \tag{3.11}$$

$$\frac{\partial \mathbf{A}}{\partial x}\Big|_{i,j} = \frac{3\mathbf{A}_{i,j} - 4\mathbf{A}_{i,j-1} + \mathbf{A}_{i,j-2}}{2\Delta y}\,. \tag{3.12}$$

The velocity gradient $\mathbf{L}$ in (2.6) is defined as the sum of the rate of deformation $\mathbf{D}$ and the vorticity $\mathbf{W}$, and is discretized based on the velocity field (3.1) as

$$\big(\mathbf{L}_{i,j}\big) = \begin{pmatrix} \frac{\partial u}{\partial x}\big|_{i,j} & \frac{\partial u}{\partial y}\big|_{i,j} & \frac{\partial u}{\partial z}\big|_{i,j} \\ \frac{\partial v}{\partial x}\big|_{i,j} & \frac{\partial v}{\partial y}\big|_{i,j} & \frac{\partial v}{\partial z}\big|_{i,j} \\ \frac{\partial w}{\partial x}\big|_{i,j} & \frac{\partial w}{\partial y}\big|_{i,j} & \frac{\partial w}{\partial z}\big|_{i,j} \end{pmatrix}\,. \tag{3.13}$$

To simulate and solve this problem, the velocity field, $(u, v)$ is directly obtained from the experimental results of the [22]. Equations (3.10), (3.11) and (3.12) are used to calculate the velocity gradient for the bulk flow, and the boundaries. Also,

according to (2.7), the discretized rate of deformation is illustrated as

$$\left(\mathbf{D}_{i,j}\right) = \begin{pmatrix} \frac{\partial u}{\partial x}\big|_{i,j} & \frac{1}{2}\left(\frac{\partial u}{\partial y}\big|_{i,j} + \frac{\partial v}{\partial x}\big|_{i,j}\right) & \frac{1}{2}\left(\frac{\partial u}{\partial z}\big|_{i,j} + \frac{\partial w}{\partial x}\big|_{i,j}\right) \\ \frac{1}{2}\left(\frac{\partial v}{\partial x}\big|_{i,j} + \frac{\partial u}{\partial y}\big|_{i,j}\right) & \frac{\partial v}{\partial y}\big|_{i,j} & \frac{1}{2}\left(\frac{\partial v}{\partial z}\big|_{i,j} + \frac{\partial w}{\partial y}\big|_{i,j}\right) \\ \frac{1}{2}\left(\frac{\partial w}{\partial x}\big|_{i,j} + \frac{\partial u}{\partial z}\big|_{i,j}\right) & \frac{1}{2}\left(\frac{\partial w}{\partial y}\big|_{i,j} + \frac{\partial v}{\partial z}\big|_{i,j}\right) & \frac{\partial w}{\partial z}\big|_{i,j} \end{pmatrix}, \tag{3.14}$$

and the vorticity (2.7) is also discretized as

$$\left(\mathbf{W}_{i,j}\right) = \begin{pmatrix} 0 & \frac{1}{2}\left(\frac{\partial u}{\partial y}\big|_{i,j} - \frac{\partial v}{\partial x}\big|_{i,j}\right) & \frac{1}{2}\left(\frac{\partial u}{\partial z}\big|_{i,j} - \frac{\partial w}{\partial x}\big|_{i,j}\right) \\ \frac{1}{2}\left(\frac{\partial v}{\partial x}\big|_{i,j} - \frac{\partial u}{\partial y}\big|_{i,j}\right) & 0 & \frac{1}{2}\left(\frac{\partial v}{\partial z}\big|_{i,j} - \frac{\partial w}{\partial y}\big|_{i,j}\right) \\ \frac{1}{2}\left(\frac{\partial w}{\partial x}\big|_{i,j} - \frac{\partial u}{\partial z}\big|_{i,j}\right) & \frac{1}{2}\left(\frac{\partial w}{\partial y}\big|_{i,j} - \frac{\partial v}{\partial z}\big|_{i,j}\right) & 0 \end{pmatrix}. \tag{3.15}$$

## 3.2 Simulation Setup

As discussed earlier, the implicit functions are written in the form of $\mathbf{A}_{i+1} = F(\mathbf{A}_{i+1}, \mathbf{A}_i)$ which has both the current and later states as the inputs of the function. These functions require determining the next step in addition to using the current step to find the $\mathbf{A}_{i+1}$ values. Thus, use of the discretized equation (3.9) is required to detect the orientational flow of the ellipsoidal grains and find $\mathbf{A}_{i+1,j}$. In this work, MATLAB is used to numerically solve the governing equations of the orientational tensors for ellipsoidal grains in a flat bottom hopper during the discharge. All the simulation setups are taken identical to the experiment setups in [22]. The hopper dimensions are considered similar to [22] experiment's hopper equal to 300mm height, 130mm width, and 150mm length. The hopper is featured with a rectangular orifice with a length equal to the width of the hopper and two different widths of 10mm and 15mm. The orientational flow of the non-spherical grains, developing in the $xy$ plane, is investigated in this work. Therefore, the two-dimensional $xy$ plane where $y$ is pointing downward is considered as the coordinate plane for the solution. The geometry of

the hopper and the meshing method are considered similar to the experimental setup in [22] hence the hopper is meshed with $78 \times 119$ nodes in the $x$ and $y$ axes, where there is an equal distance of 1.712mm between each cell in both the $x$ and $y$ directions. Each cell is identified by $i$ and $j$ for $x$ and $y$ axis, respectively. The $j$ and $i$ increase toward the right side and downward of the hopper, respectively. The hopper characteristics can be seen in Figure (3.1).

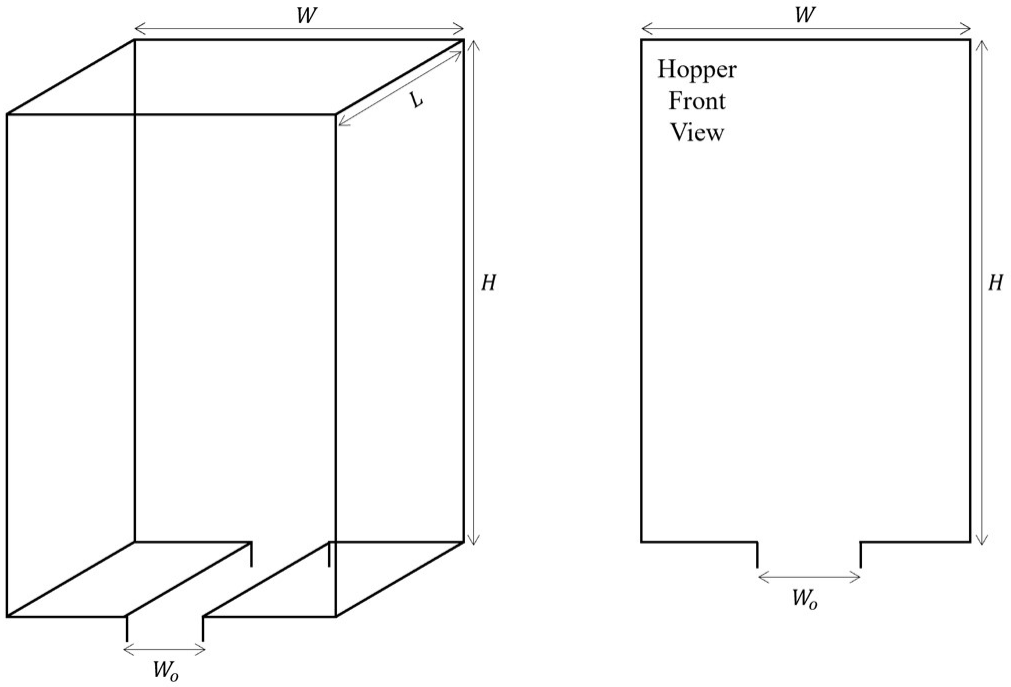


Figure 3.1: Geometry of the flat bottom hopper employed for the kinematic model simulations. Width, length and height of the hopper are 130mm, 150mm and 300mm, respectively. Two different width sizes for the openings as $W_o = 10, 15$mm are considered in the simulations.

To numerically solve the model, the $xy$ plane velocity field is taken from the [22]. The velocity gradients, rate of deformation, and vorticity for the flow in hopper are calculated from velocity field. To avoid stagnation zones building up in the corners during flow discharge, the numerical analysis is performed in the center of the hopper, where there is a significant flow which is required for the model to predict

the orientation field of the grains.

The "fsolver", a function in MATLAB, is used to solve this system of unconstrained, nonlinear equations. This solver takes the velocity field and orientation of each node and uses them to numerically solve the equations and find the values of the next nodes which are used to solve for the next layer of the nodes in the same way.

To solve the ordinary differential equations in (3.9), a starting point must be specified. Therefore, the orientation field of the grains at the highest layer of the hopper is only taken from the experimental setup available in [22] as the starting point. The experimental measurements have been determined in a 2-D plane while the kinematic model predicts the orientation field of grains in a 3-D space. Hence a transition from the 2-D plane of $xy$ to 3-D space of $xyz$ for the orientation field is required. The orientation fields from the experiments are two-by-two matrices; by adding the third dimension, they become three-by-three tensors. The sum of the main diagonal elements of the tensors, which is the trace of the tensor, for the model is considered to be equal to one. Therefore, the diagonal arrays $A_{11}$, $A_{22}$ and $A_{33}$ of the model are determined in a way to keep the trace of all orientational tensors equal to one, and also stay similar to the initial tensors after transformation. The following transition is used to project the orientation field in the $z$ direction

$$\begin{aligned} \mathbf{A}_{\text{Exp}} = \begin{pmatrix} A_{11} & A_{12} \\ A_{21} & A_{22} \end{pmatrix} \Rightarrow \mathbf{A}_{\text{Mod}} &= \begin{pmatrix} A'_{11} & A'_{12} & 0 \\ A'_{21} & A'_{22} & 0 \\ 0 & 0 & A'_{33} \end{pmatrix} \\ \Rightarrow \mathbf{A}_{\text{Mod}} &= \begin{pmatrix} A_{11} + \frac{1}{2} - \frac{A_{33}}{2} & A_{12} & 0 \\ A_{21} & A_{22} + \frac{1}{2} - \frac{A_{33}}{2} & 0 \\ 0 & 0 & A_{33} \end{pmatrix}, \end{aligned} \tag{3.16}$$

where $\mathbf{A}_{\text{Exp}}$ and $\mathbf{A}_{\text{Mod}}$ indicate the experiment and model tensors, respectively. In the experiment [22], the trace of the experimental tensors were scaled to be equal to zero, such that $A_{11}$ is equal to $-A_{22}$. By defining $A_{33}$ equal to $A_{11} - A_{22}$, the trace remains zero. Moreover, adding 1/2 to $A_{11}$ and $A_{22}$, also subtracting $A_{33} = (A_{11} - A_{22})/2$ from those two, can make the trace equal to one. Since the orientation of the grains does not change through the $z$ direction the components of the model tensor are considered to be equal to zero.

The tensors derived from (3.16) are considered as the 3-D starting points for solving the model numerically. These initial tensors are only employed for the first layer of the equation. Afterwards, the solution adopts the previous layer tensors to continue and solve the model. All the model calculation results and the comparison with experimental results are discussed in the chapter (4).

## 3.3 Model Generalization

The parameters $\lambda$ and $\psi$, which are introduced in chapter 2.1, are model parameters and need to be determined by experiment. Nadler et al. in [21] determined them from DEM simulations in homogeneous steady-state simple shear flow. As discussed earlier, the model parameters in [21] were considered to be only the functions of the shape ratio as stated in equations (2.15). Therefore, the $\lambda$ and $\psi$ were defined as

$$\lambda = \hat{\lambda}(r_g), \qquad \psi = \hat{\psi}(r_g)\,. \tag{3.17}$$

After investigating the model performance and comparing the model calculations with the experimental results of [22], it was found that the model is not in a good agreement with the experiment in capturing the orientation of the grains. Since the shapes of the grains are important factors that affect the orientation field and

mechanical responses, proposing a model that can capture the orientation of the non-spherical grains is the main objective of this work. Therefore, the model parameters are generalized to extend its performance.

The model parameters can depend on all of the objective characteristics of the system such as grain shape and size, deformation rate, mutual alignment, orientational tensor and other factors. However, to better capture the effect of the grain shape on the flow, model parameters should be a function of orientational tensor $\mathbf{A}$. The invariants of the orientational tensor $\mathbf{A}$ are considered among its dependent functions. Employing invariants as the model parameter equations along with the kinematic model would be beneficial since not only they are functions of the tensor, but also they will not undergo any change due to the rotations of the coordinate system.

In the current kinematic model, by using an extension of the eigenvalues as the invariants to capture the grain alignment, [21] proposed the level of mutual alignment also known as ordering measure. It is defined by $\zeta$ as

$$\zeta = \sqrt{\frac{1}{2}\big((\alpha_1 - \alpha_2)^2 + (\alpha_2 - \alpha_3)^2 + (\alpha_3 - \alpha_1)^2\big)}\,, \tag{3.18}$$

where $0 \leq \zeta \leq 1$. The case $\zeta = 0$ demonstrates the isotropic distribution of the grains, where all the eigenvalues are $\alpha_1 = \alpha_2 = \alpha_3 = 1/3$. On the other hand, $\zeta = 1$ represents the maximum alignment of the grains when all the grains are aligned along one direction, where two of the eigenvalues are zero, and the other one equals to one.

In [21] it was observed that the ordering measure is strongly influenced by grain shape. The grain alignment increases for more ellipsoidal grains and decreases for more spherical grains. Furthermore, $\zeta$ is a scalar invariant of the orientational tensor $\mathbf{A}$. Therefore, having it as one of the dependencies of the model parameters adds valuable information to the kinematic model results. Thus, the equations in (3.17)

are considered to be the functions of the shape ratio and $\zeta$ as

$$\lambda = \hat{\lambda}(r_g, \zeta(\mathbf{A})), \qquad \psi = \hat{\psi}(r_g, \zeta(\mathbf{A}))\,. \tag{3.19}$$

However, for simplicity, the proposed model is limited to the simplest case where the model parameters are linear in $\zeta$ and $r_g$.

As discussed the $r_g$ is changing between $-1$ and 1. It vanishes for spherical grains. Also, it is positive and increasing with the larger dimension for prolate grains, and negative and decreasing for oblate grains. The $\lambda$ values are increasing between $-1$ and 1, while $\psi$ and $\zeta$ values are positive and changing between 0 and 1. Therefore, it is expected to have the following values for $\psi$ and $\lambda$ as they are considered to be the linear functions of $\zeta$ and $r_g$

$$\begin{cases} r_g > 0: \;\; 0 < \lambda < 1, \;\; 0 < \psi \\ r_g < 0: \;\; -1 < \lambda < 0, \;\; 0 < \psi \end{cases}. \tag{3.20}$$

According to (2.15), two linear dependencies are proposed to capture the (3.20) values and improve the model performance as

$$\begin{cases} \lambda(r_g, \zeta) = \big(\lambda_a \zeta + \lambda_b (1-\zeta)\big) r_g \\ \psi(r_g, \zeta) = \big(\psi_a\, \zeta + \psi_b (1-\zeta)\big) \big|r_g\big| + \psi_c \end{cases}. \tag{3.21}$$

As discussed earlier, the experiment results in [22] are considered as the baseline for investigating the model performance, model generalization and improvement. Therefore, in this work the components of the model parameters of $\lambda_a$, $\lambda_b$, $\psi_a$, $\psi_b$ and $\psi_c$, for the generalized model, are found such that the prediction of the model becomes as close as possible to the experiment. To achieve this goal, an optimization method

is needed to minimize the differences between the model and experiment considering the conditions in (3.19), (3.20) and (3.21).

The function for optimizing the model parameters can be proposed by using the norm of the differences of the orientational tensors of the model and experiment at each point. However, this function is difficult to optimize since nine variables are included in the optimization. However, the angles of the grains with the horizontal axis and the ordering are the functions of the orientational tensors. Therefore, the angle of the grains with the horizontal axis and the ordering measure can be taken as parameters that present the characteristics of the orientational tensors. As a result, a function is taken, using the differences between the calculated angles and ordering parameters of the model and experiment tensors. This function is defined as

$$\mathrm{Err}_1 = \theta_{\mathbf{A}_{\mathrm{Mod}}} - \theta_{\mathbf{A}_{\mathrm{Exp}}} ,$$

$$\mathrm{Err}_2 = \zeta_{\mathbf{A}_{\mathrm{Mod}}} - \zeta_{\mathbf{A}_{\mathrm{Exp}}} ,$$

$$\mathrm{Err} = \sum_{\mathrm{i}} \sum_{\mathrm{j}} \left( \left| \mathrm{Err}_1 / 2\pi \right| + |\mathrm{Err}_2| \right) ,$$

where i and j are the notations for the entire rows and columns of the grains in the hopper. Also, the $\mathrm{Err}_1$ value is within the $-\pi$ to $+\pi$ and $\mathrm{Err}_2$ value is within $-1$ and 1, therefore first equation is divided by $2\pi$ to be added to the second equation value, such that sum is unitless. Also, the Err function calculates the $\mathrm{Err}_1$ and $\mathrm{Err}_2$ for all of the tensors within the domain of the hopper. Finally, the values of all of the tensors in the rows and columns of the hopper are added together to minimize the total value of differences.

The algorithm in Figure (3.2) is employed to optimize the Err function and find the best fit of $\lambda_a$, $\lambda_b$, $\psi_a$, $\psi_b$ and $\psi_c$. According to the algorithm in Figure (3.2), an initial value is required as the starting point for each of the $\lambda$ and $\psi$ components to

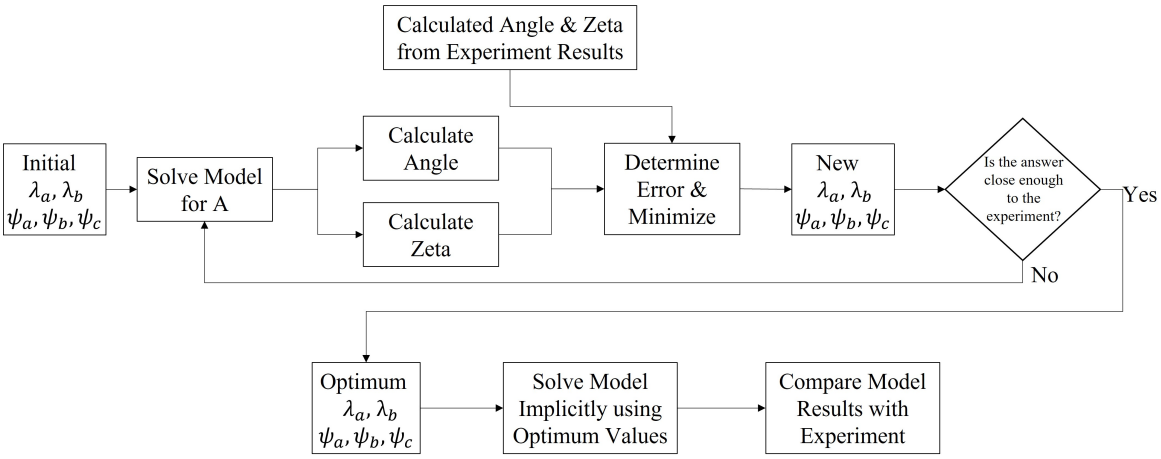


Figure 3.2: Algorithm used to find the best values for $\lambda_a$, $\lambda_b$, $\psi_a$, $\psi_b$ and $\psi_c$.

start the optimization process. The choice of a starting point determines how quickly the algorithm converges to a minimum. Therefore, choosing an initial value close to the expected result helps the solution to converge to the result faster.

To ensure the performance of the proposed models of (3.21), and to find the best starting point, the $\lambda$, $\psi$, $r_g$ and $\zeta$ values for various grains that were provided in [21] are employed to draw the spatial curves of $\lambda$ and $\psi$ with respect to $\zeta$ and $r_g$ using curve fitting. The values provided in [21] include the shape ratio of only a few types grains with homogeneous characteristics of specified ordering and relaxation measures. According to values in [21] and (3.21), two figures of $\lambda(r_g, \zeta)$ and $\psi(r_g, \zeta)$ are fitted and shown in Figures (3.3) and (3.4). Also, the initial values of $\lambda_a$, $\lambda_b$, $\psi_a$, $\psi_b$ and $\psi_c$, required to start the optimization algorithm of Figure (3.2), are determined from curve fittings.

Figures (3.3) and (3.4) represent the two proposed models of (3.21) for homogeneous results. It can be observed that the proposed models are already capable of covering the values of $\lambda$ and $\psi$ for different types of grains with their specified ordering factors. In other word, two proposed models in (3.21) show a good agreement with [21] for the particular case of homogeneous data. However, the performance of the

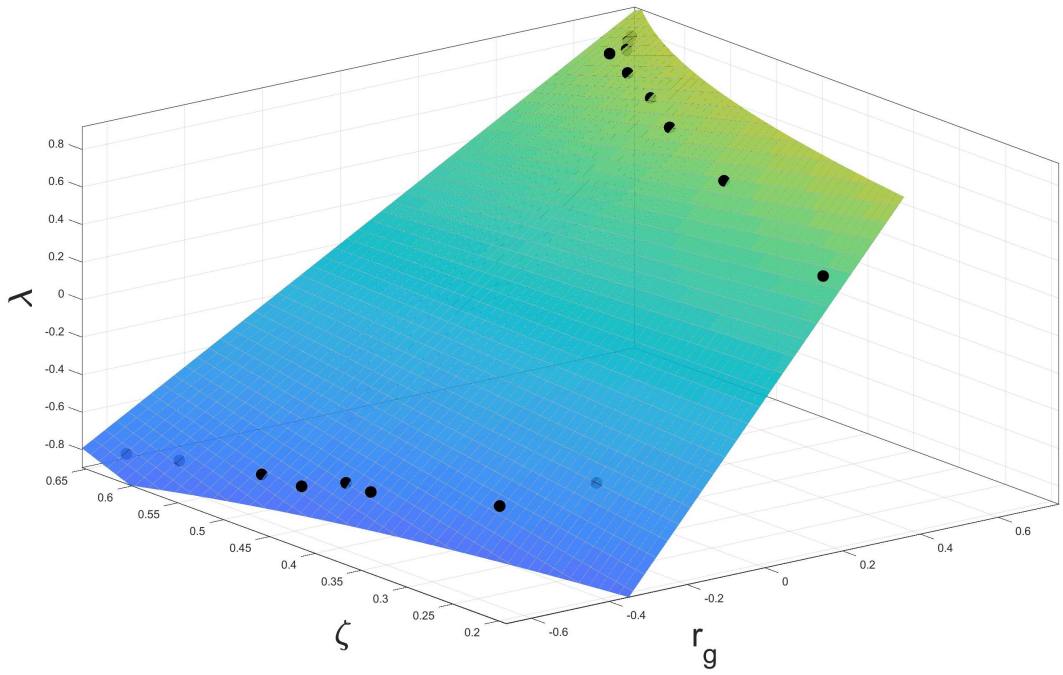


Figure 3.3: Figure of $\lambda(r_g, \zeta)$ taken from curve fitting, using the values of $\lambda$, $r_g$ and $\zeta$ from [21] to show the performance of the proposed model of $\lambda$ with homogeneous data.

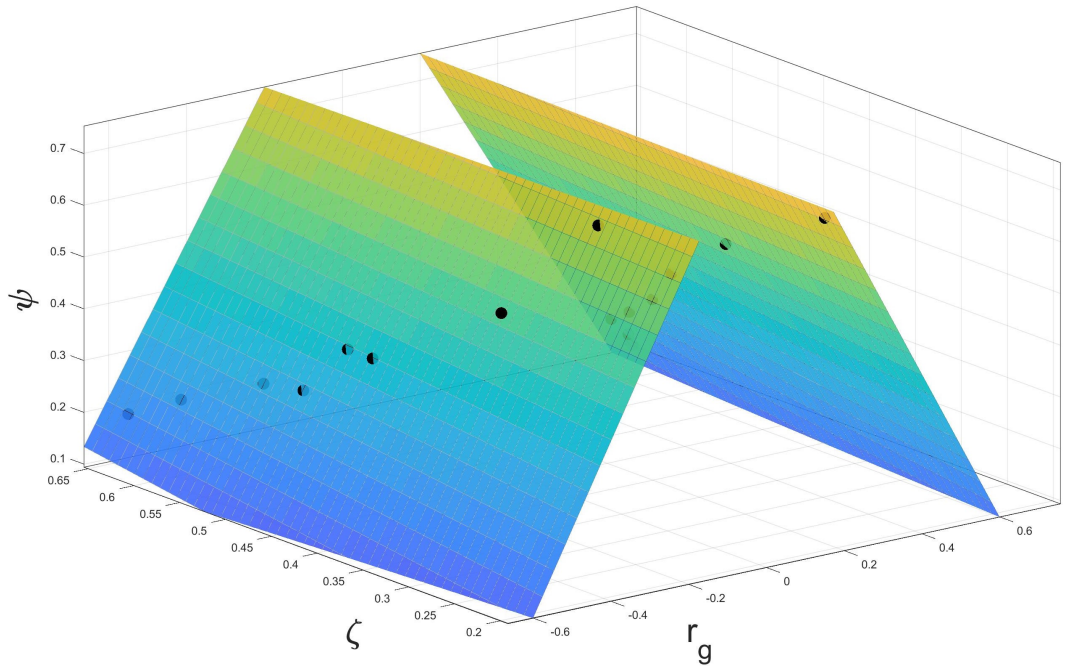


Figure 3.4: Figure of $\psi(r_g, \zeta)$ taken from curve fitting, using the values of $\psi$, $r_g$ and $\zeta$ from [21] to show the performance of the proposed model of $\psi$ with homogeneous data.

proposed models of $\lambda$ and $\psi$ should be investigated for inhomegenous flow in hopper discharging as well to ensure the accuracy of the model.

# Chapter 4

# Results and Discussions

This chapter contains an explanation of the result visualization method on a 2-D plane. It defines the domain and the aspect ratios of the grains used for simulations. Also, it presents the model performance investigation and the analysis. A comparison between the model performance investigation results and the experimental results is given to show the model feasibility. Afterwards, the generalized model results and analysis show the improvement visually. Finally, an error function is proposed to quantify the differences between the generalized model and experimental results, also the model itself.

## 4.1 Orientation Distribution Visualization Method

The orientational fields are calculated by applying the discretized equation (3.9) in the hopper. To visualize and compare the calculated domain with the two-dimension experimental results, a transition from 3-D space to the 2-D plane is needed to prepare the model results for visualization. A backward transition opposite to (3.16) is employed to obtain the 2-D orientational tensors as

$$\mathbf{A}_{\text{Mod 3-D}} = \begin{pmatrix} A'_{11} & A'_{12} & 0 \\ A'_{21} & A'_{22} & 0 \\ 0 & 0 & A'_{33} \end{pmatrix} \Rightarrow$$
$$\mathbf{A}_{\text{Mod 2-D}} = \begin{pmatrix} A'_{11} & A'_{12} \\ A'_{21} & A'_{22} \end{pmatrix} + \frac{A'_{33}}{2} \begin{pmatrix} 1 & 0 \\ 0 & 1 \end{pmatrix} , \tag{4.1}$$

where the $A'_{ij}$ are the arrays of the orientational tensors calculated by the kinematic model. According to the [22] a transition used to prepare the experimental results for visualizing as

$$\mathbf{A}_{\text{Exp}} = \begin{pmatrix} A_{11} & A_{12} \\ A_{21} & A_{22} \end{pmatrix} \Rightarrow$$
$$\mathbf{A}_{\text{V}} = \frac{\mathbf{A}_{\text{Exp}}}{\sqrt{2}} + \frac{1}{2} \begin{pmatrix} 1 & 0 \\ 0 & 1 \end{pmatrix} , \tag{4.2}$$

where $\mathbf{A}_{\text{V}}$ is the representation for the visualized orientational tensors of the experiment.

The ellipsoidal grains are the intended grains of this study. Therefore, rice as the prolate and lentil as the oblate grains are employed to find out the impact of the shape of the non-spherical grains on the orientation. The aspect ratios of both grains

are provided by the experiment [22] and can be found in Table (2.1).

According to [22], eigenvalues and eigenvectors of the tensors represent the elongation and orientation of the grains. In a 2-D plane, the smaller eigenvalue shows the ellipse width, and the larger eigenvalue shows the ellipse length. Since the ellipsoidal grains are employed to calculate the orientational field, an oval shape is used to visualize the grains. Similarly, the larger eigenvalue is therefore used to find the length of the ellipsoidal shapes, and the smaller eigenvalue is used to calculate the width of the oval shapes. Also, the eigenvector associated with the length of the shape is used to find the orientation angle of each grain. Since, each orientational tensor has two eigenvalues of $\alpha_1$ and $\alpha_2$ and two eigenvectors as $\mathbf{a}_1$ and $\mathbf{a}_2$. Using the components of the eigenvector associated with the length, the angle of the grains against the horizontal axis can be defined as follows

$$\theta_{\text{Oval}} = \tan^{-1}\left(\frac{\mathbf{a}_1^y}{\mathbf{a}_1^x}\right), \tag{4.3}$$

where $\mathbf{a}_1^y$ and $\mathbf{a}_1^x$ are the components of the associated eigenvectors, in $y$ and $x$ directions respectively, to the larger aspect of the grains. Figure (4.1) is a representation of a non-spherical grain that is used in the model investigation and generalization. It

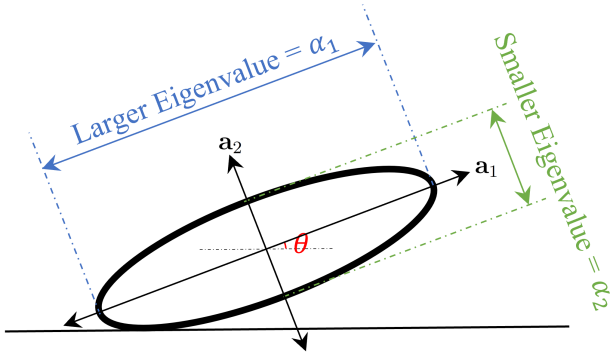


Figure 4.1: Eigenvalues and Eigenvectors of each grain used to find the angle between ovals and horizontal axis. $\mathbf{a}_1$, $\mathbf{a}_2$ and $\theta$ are the eigenvectors and angle between the larger eigenvector and horizontal line, respectively.

is showing both the eigenvalues and their associated eigenvectors are employed to find the angle between each grain and the horizontal axis. The values shown in Figure (4.1) are used to sketch the 2-D oval shapes available in all the layers of the hopper.

## 4.2 Model Performance Results and Discussion

Experimental results in [22] were determined for the entire hopper area. However, to minimize the errors of the imaging, a smaller field is provided in the results. Therefore, the experimental data is available from 7mm to 191mm in the height of the hopper, also from 10mm to 108mm in the width of the hopper.

To capture the principal angle field, the kinematic model in [21] is used for all the layers in both directions of $x$ and $y$ according to the results provided in the experiment. The results are visualized for 80mm below the highest layer of the grains in the hopper and 3mm above the opening of the hopper. Thus, the visualized domain is considered to be from 80mm to 188mm in the $y$-axis, and 29.25mm to 81.75mm in the $x$-axis to have a more representative result and neglect the stagnation zones. Furthermore, according to Figure (3.1), the center of both openings is placed at the zero point to capture and represent the orientations of the grains that happen in the flow during discharge.

The angle field of the experimental results [22] for rice and lentil discharging through two different size openings are shown in the Figures (4.2a) to (4.2d). Figures (4.2a) and (4.2b) visualize the principal angle fields of the rice discharging through 10mm and 15mm openings for the analyzed domain. The color maps demonstrate the angle between the grains and the horizontal axis everywhere during the discharge through both openings. From comparing the flow streams of the two openings, it can be concluded that grain orientation starts at upper layers for the smaller opening.

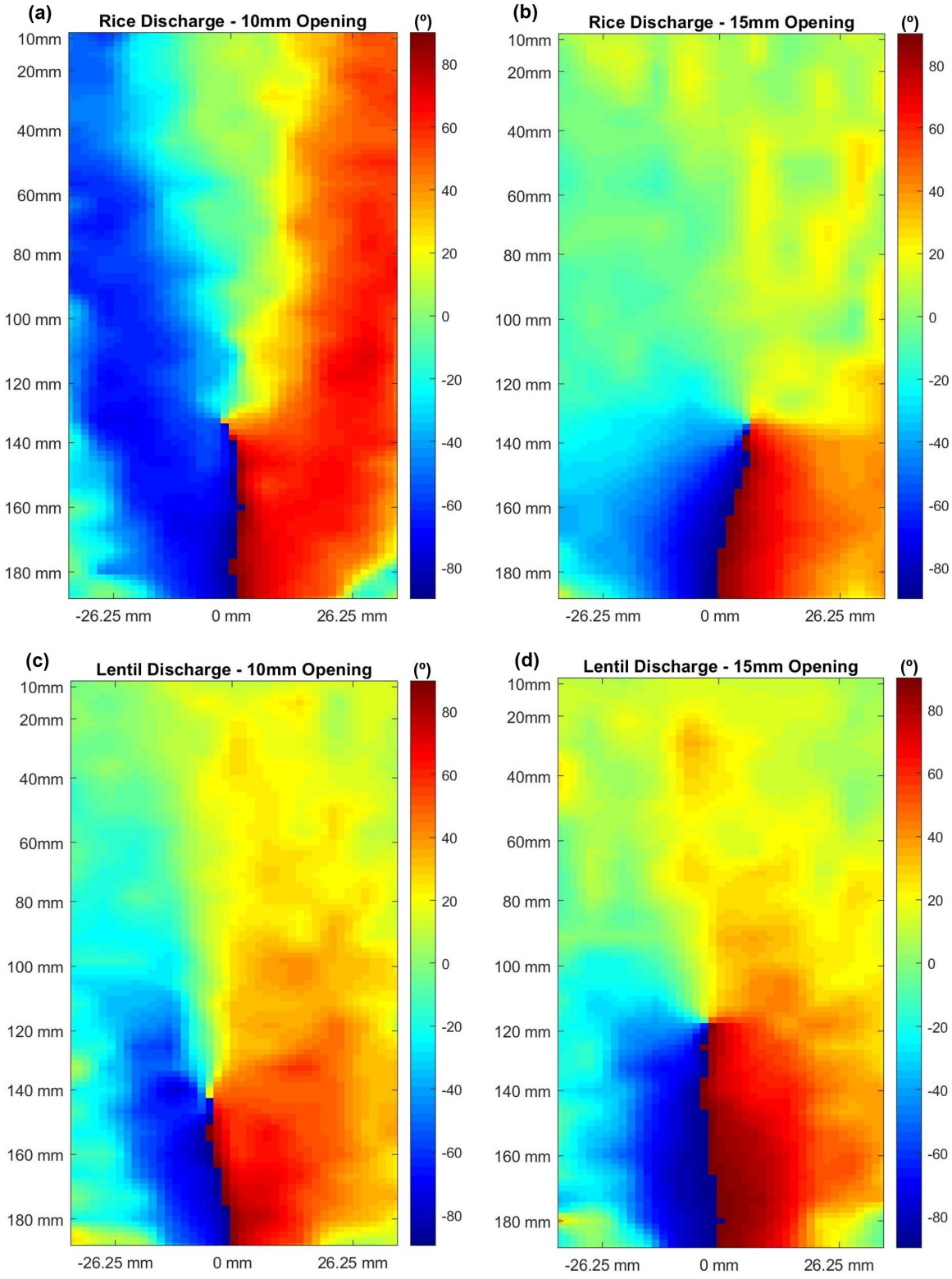


Figure 4.2: Principal angle domain of experimental results of [22]; Rice and Lentil discharges through 10mm and 15mm openings. The color bars provided for all four figures are showing the degree ranges of all the grains within $-90$ to 90 degrees. a) and b) show Rice discharge, c) and d) show Lentil discharge through 10mm and 15mm openings, respectively.

Furthermore, it can be observed that the grains are approaching the center of the opening for both openings at different angles. This means that at discharging time in the middle part of the hopper, grains rotate towards the center of the openings with positive and negative principal directions and align vertically with each other. Also, the zones with lower velocities such as stagnation zones can be seen in the color maps of the angle domains at the edges of the hopper.

Figures (4.2c) to (4.2d) visualize the angle fields of the lentil discharging through 10mm and 15mm openings for the analyzed domain. Like rice, lentils start to orient at upper layers at the time of discharge from the smaller opening. Furthermore, similar to the rice grains, lentil grains are more aligned with the flow streams and each other in the middle of the hopper. They also reorient themselves toward the center of the opening with positive and negative principal directions.

Comparing the rice and lentil principal angle fields show that the orientation of lentil starts at the upper layers compared to rice. It leads to the conclusion that rice grains have a more ellipsoidal shape compared to the lentils, that cause them to orient with the flow slower. In addition, it can be seen from color maps that funnel flow takes place in the hopper for the smaller opening, while bulk flow occurs in the hopper for the larger opening. It can be observed that in the upper layers, grains are typically lying horizontally due to the filling procedure. Moreover, in the bulk flow, grains start to align with the flow stream when they reach the openings. However, in the funnelling flow, grains begin to align at farther upstream from the middle of the hopper.

### 4.2.1 Comparison of the Model Performance and Experiment

As discussed in section (4.1), a similar method is used to visualize the model results. Also, to compare the experiment and the model, the same structure is used to sketch the principal angle domains. Figures (4.3a) to (4.3d) visualize the angle fields of the rice and lentil discharging through 10mm and 15mm openings for the analyzed domain of the model calculations. The color maps demonstrate the angle between the grains and the horizontal axis during the discharge through both openings. Color maps are only presenting the middle 29.25mm to 81.75mm width of the hopper since the stagnation zones in the side of the hopper have been neglected for the model calculations.

Figures available in (4.2) and (4.3) demonstrate the angle domain of the experiment and model results for both openings. By comparing the angle domains, it can be observed that the model prediction is less effective in capturing the distribution of the grains during the flow down the hopper compared to the experiment. However, the location and the orientation of the grains at the highest layer of the hopper are considered identical in model simulation and experiment. The prediction of the model shows that reorientation of the grains starts farther upstream for both openings compared to the experiment. Unlike the experiment, the model is not able to distinguish the funnelling and bulk flow that typically happens due to the smaller and larger openings, respectively. Moreover, the model is not capable of detecting the zones in which grains have lower velocities such as the edges of the hopper, while the experiment results present these zones in both edges of the hopper and upper streams. The effect of the collision of the grains, which cause the grains to be misaligned from the flow stream, is captured less in the model calculations than in the experimental results. This means that the grains in the model results are more aligned with respect to each

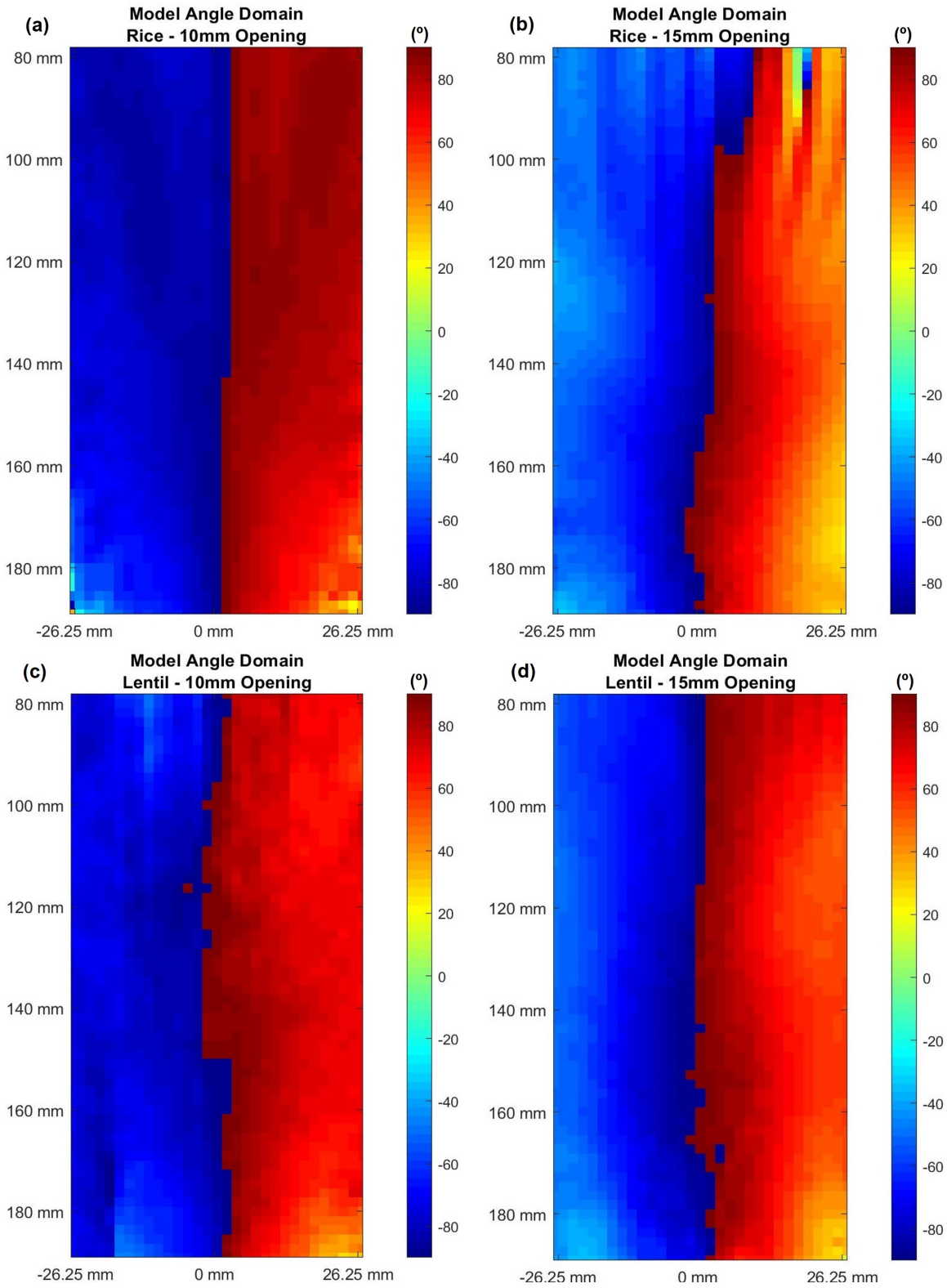


Figure 4.3: Principal angle of model calculations; Rice and Lentil discharges through 10mm and 15mm openings. The color bars provided for all four figures are showing the degree ranges of all the grains within $-90$ to 90 degrees. a) and b) show Rice discharge, c) and d) show Lentil discharge through 10mm and 15mm openings, respectively.

other and the flow compared to the experiment. It is observed that the orientation field of rice and lentil, obtained by the model, matches better to the experimental measurements in the middle of the hopper near the openings in comparison to the edges of the hopper. This indicates that the model can predict the orientation field for the locations with significant flow. Moreover, from comparing angle domains of lentil and rice discharges, it can be concluded that both rice and lentil grains reorient towards the center of the openings according to their larger eigenvalues. Overall, the model calculations are not showing a good agreement with the experimental results in an inhomogeneous flow.

### 4.2.2 Generalized Model Performance Results Comparison with Model and Experiment

The intention of having model parameters $\lambda$ and $\psi$ as the functions of shape ratio $r_g$, and ordering parameter $\zeta$, was explained earlier. Also, the method of improving the model parameters $\lambda$ and $\psi$ was discussed in Chapter 3 Section 3. The values in table (4.1) for $\lambda_a$, $\lambda_b$, $\psi_a$, $\psi_b$ and $\psi_c$ are determined from optimization for the proposed model parameters of (3.21).

| **Model Parameter** | $\lambda_a$ | $\lambda_b$ | $\psi_a$ | $\psi_b$ | $\psi_c$ |
|---|---|---|---|---|---|
| **Value** | 0.17609 | 2.1336 | -1.1723 | -1.4416 | 1.3951 |

Table 4.1: Values of the generalized model parameters.

Therefore the following equations can be used as the model parameters along with the kinematic model of (2.12) to calculate the orientation distribution of the grains

$$\begin{cases} \lambda(r_g,\zeta) = \big(0.17609\zeta + 2.1336(1-\zeta)\big) r_g \\ \psi(r_g,\zeta) = \big(-1.1723\zeta - 1.4416(1-\zeta)\big)\big|r_g\big| + (1.3951) \end{cases} . \tag{4.4}$$

As discussed in section (4.1), a similar method is used to visualize the generalized model results. Also, to be able to compare the experiment, model and generalized model with each other, the same structure, as declared earlier, is used to sketch the oval shape of the grains for the experiment, model and generalized model results. However, all the calculations take place in the analyzed domain, the orientations of the grains and ovals are only presenting within the bottom part of the analyzed domain from 160mm to 188mm in $y$-axis and the entire $x$-axis to be more representative. Figures (4.4a) to (4.4d) and (4.5a) to (4.5d) demonstrate the comparison of the orientation field of the experiment with the model and generalized model for rice and lentil discharges through 10mm and 15mm openings, respectively. In the orientational domain figures, blue ovals demonstrate the orientational field of the experimental results, and red ovals represent the model or the generalized model results in the related figures.

From Figures (4.4) and (4.5), it can be seen that the distribution of both rice and lentil during discharging through two openings are more similar between the generalized model and experimental results compared to model and experiment. It can be observed that the ovals of the grains, in the generalized model results, better match the ovals of the grains in the experimental results compared to the model. This means that, the location and the orientation of the grains in the generalized model better follow the experimental results. Also, the effect of the collision of the grains which lead them to misaligned from the flow direction, is more captured in the generalized model compared to the model. Similar to the experiment, rice and lentil grains approach towards the center of openings with the positive principal angle on the right side and the negative principal angle on the left side of the hopper. Both rice and lentil orient according to their longer aspect. Also, the generalized model captures the funnelling and bulk flows of the grains, affected by the smaller and bigger

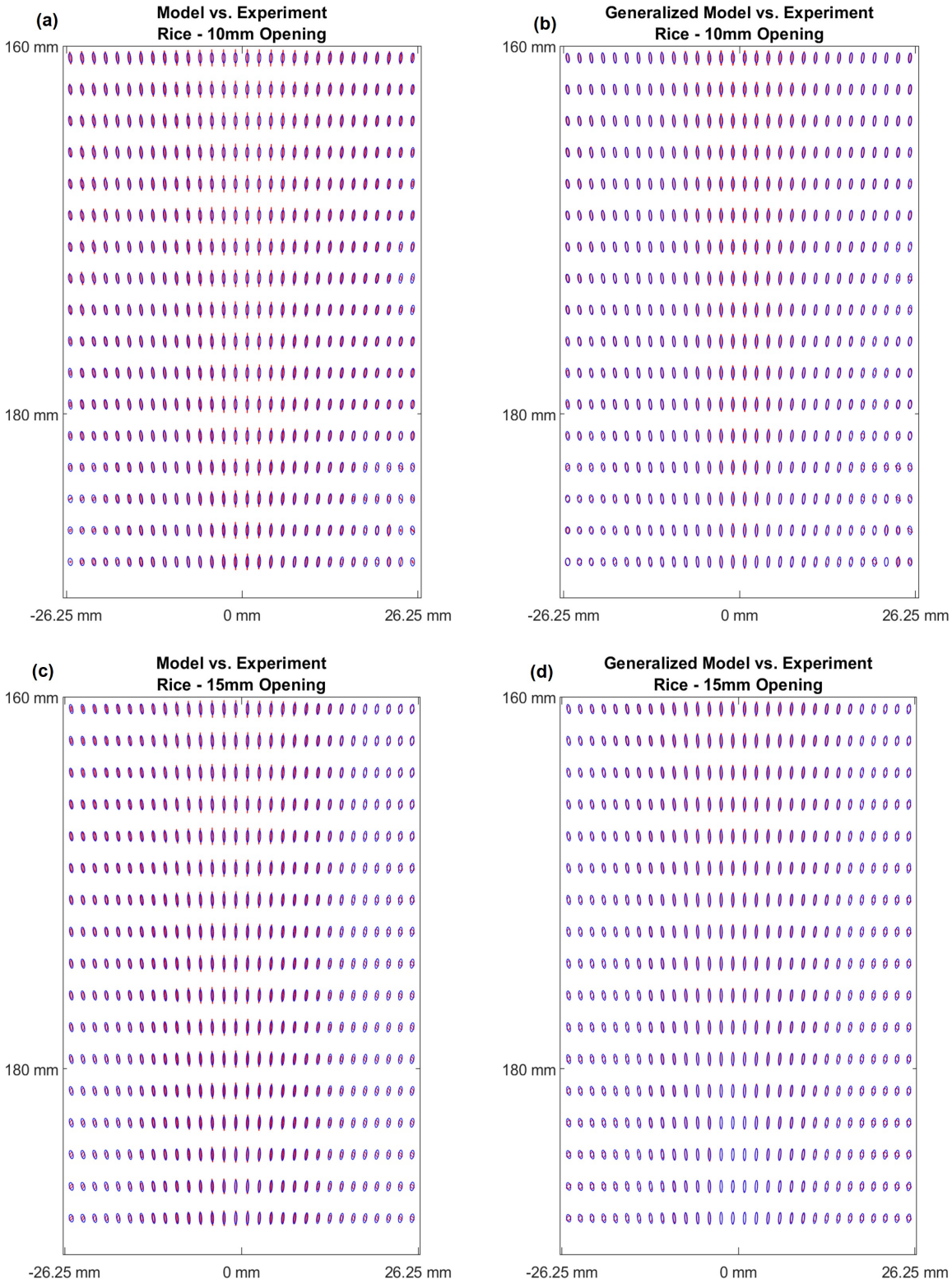


Figure 4.4: Comparison of the orientational domain of experimental results of [20], model and generalized model calculations; Rice discharges through 10mm and 15mm openings. Blue and red ovals show the experiment, model and generalized model results, respectively. a) and c)Experiment vs. Model results, b) and d)Experiment vs. Generalized model results.

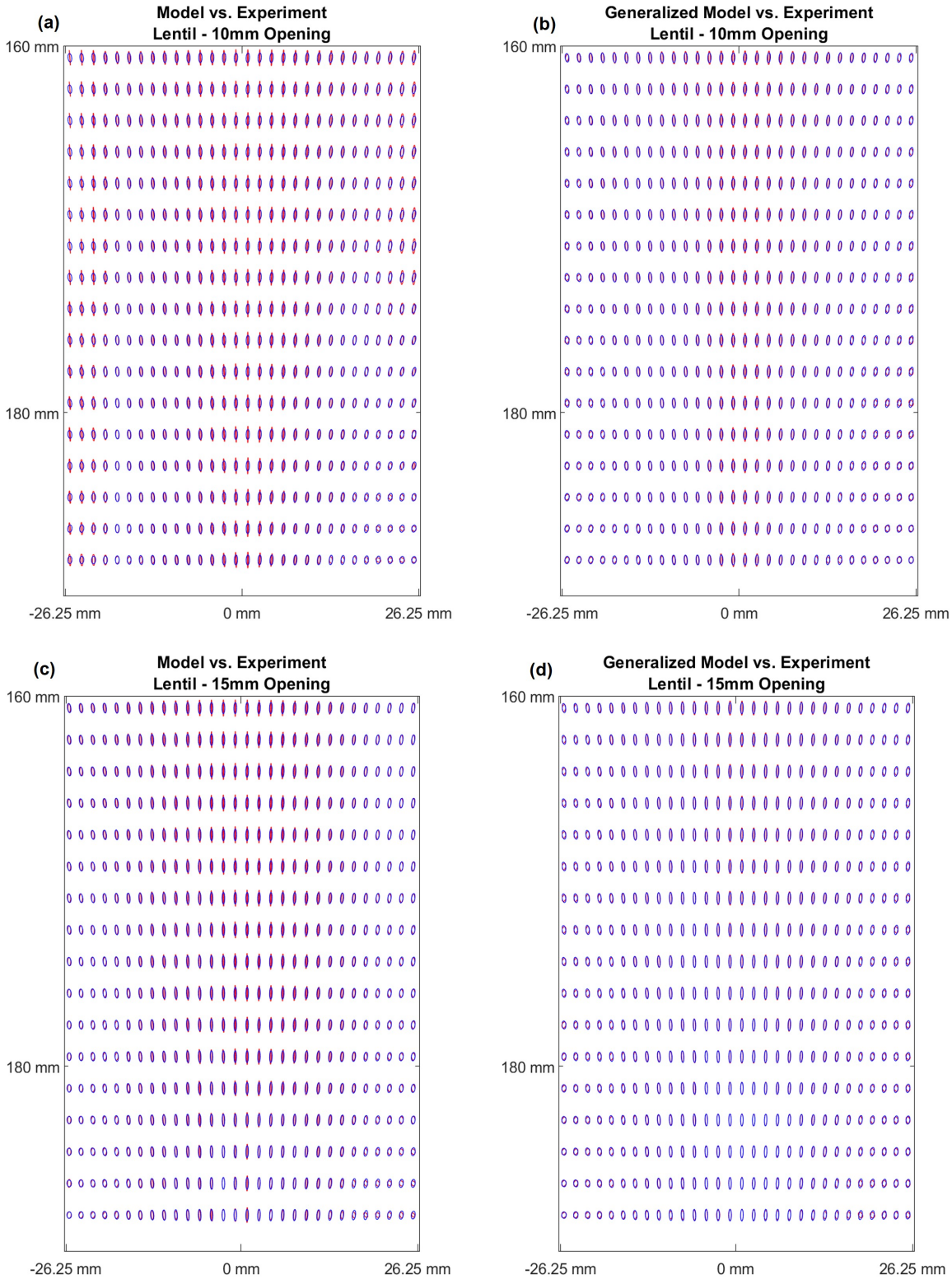


Figure 4.5: Comparison of the orientational domain of experimental results of [20], model and generalized model calculations; Lentil discharges through 10mm and 15mm openings. Blue and red ovals show the experiment, model and generalized model results, respectively. a) and c)Experiment vs. Model results, b) and d)Experiment vs. Generalized model results.

openings, more effectively compared to the model. The funneling flows for both lentil and rice discharges can be seen in Figures (4.4b) and (4.5b), and the bulk flow for both grain discharges can be seen in Figures (4.4d) and (4.5d). Also, unlike the model results, the zones with lower velocities and vertically oriented grains are more vivid in both edges of the hopper, which means that the generalized model is more successful in capturing orientation of the grains in the zones with lower velocities compared to the model.

Overall, the generalized model demonstrates a better agreement with the experimental results in calculating and capturing the orientational field in an inhomogeneous flow by carrying both $\zeta$ and $r_g$ as the components of model parameters.

### 4.2.3 Improvement Quantification

The results obtained from solving the model and the generalized model in the hopper compared to the experiment results, were qualitatively shown in the previous section. The norm of the differences of the orientational fields, divided by the norm of the orientational field of the experiment, is used to quantify the improvement between the model and the generalized model. Therefore, the quantitative comparison is calculated using the orientation tensors of the analyzed domains. As it was discussed in section (4.2), the analyzed domain is equal to 7mm to 188mm in the $y$-axis and 29.25mm to 81.75mm in the $x$-axis, which are equal to 5 to 110 rows of nodes in the height of the hopper and 25 to 55 columns of nodes in the width of the hopper. Thus, the errors for each case are calculated according to

$$\mathrm{E}_{\mathbf{A}} = \frac{1}{3286} \sum_{i=5}^{110} \sum_{j=25}^{55} \frac{\left\| \mathbf{A}_{\mathrm{Exp},ij} - \mathbf{A}_{\mathrm{k},ij} \right\|}{\left\| \mathbf{A}_{\mathrm{Exp},ij} \right\|}, \tag{4.5}$$

where $\mathbf{E_A}$ is calculated for each case of model and generalized model separately. Also, the $\mathbf{A}_{\mathrm{Exp},ij}$ shows the orientational tensors of the experiment, and $\mathbf{A}_{\mathrm{k},ij}$ represents the orientational tensors of the model or the generalized model at each node. The differences in the orientational domains can be seen in Table (4.2). The values in Table (4.2) show the difference percentage of the orientational domain of the model and generalized model compared to the experiment, where smaller values show better agreement with the experimental results.

| **Grain Type** | **Rice** | | **Lentil** | |
|---|---|---|---|---|
| **Opening Width** | 10 mm | 15 mm | 10 mm | 15 mm |
| $\mathbf{E}_{\mathbf{A}_{\mathrm{Model}}}$ | 53.67% | 34.76% | 26.57% | 26.83% |
| $\mathbf{E}_{\mathbf{A}_{\mathrm{Generalized\ Model}}}$ | 35.78% | 28.41% | 13.86% | 17.31% |

Table 4.2: Comparison of the performance of the model and generalized model calculations using the norm of the differences between the orientational domain of the experiment and the model, as well as the generalized model divided by the norm of the orientational domain of the experiment.

According to Table (4.2), the improvement percentage is calculated by deducting the generalized model error from the model error then dividing the result by the model error for all the grains and openings.

| **Grain Type** | **Rice** | | **Lentil** | |
|---|---|---|---|---|
| **Opening Width** | 10 mm | 15 mm | 10 mm | 15 mm |
| **Improvement** | 33.33% | 18.26% | 47.83% | 35.48% |

Table 4.3: Improvement of the generalized model compared to the model.

The values in Table (4.3) show the improvement percentage of the generalized model prediction compared to the model. The average improvement for discharging both lentil and rice through 10mm and 15mm openings is almost 33.725%.

Equation (4.5) is employed to calculate the differences between orientational domains of the experiment and model results, as well as the experiment and generalized model results. Figures (4.6) to (4.7) represent the color-maps of the error domain for

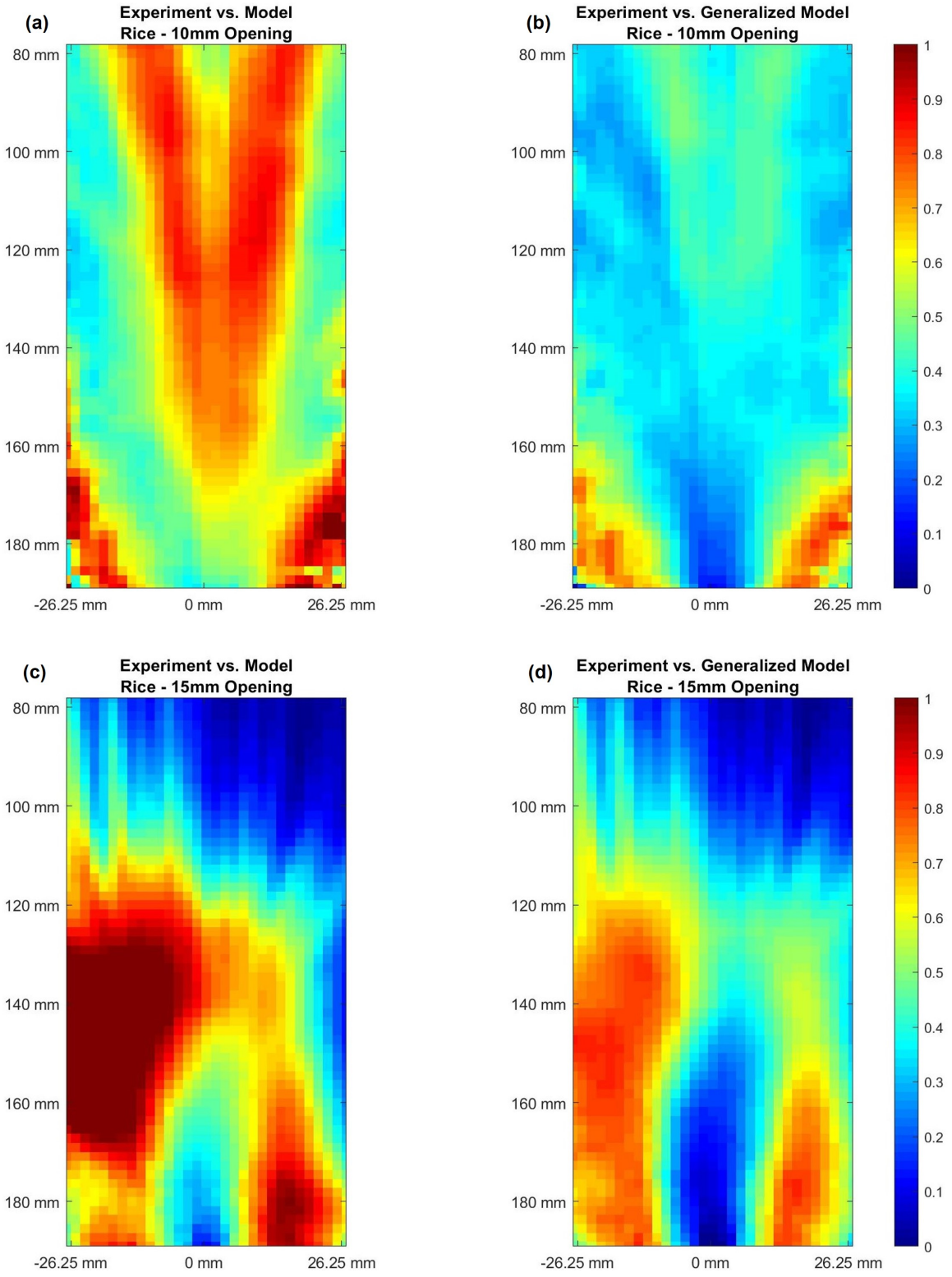


Figure 4.6: Difference percentage of the experiment, model and generalized model results of the orientational domain of Rice discharge through 10mm and 15mm openings. The color bars provided for all four figures are showing the difference ranges between the orientational domains between 0% and 100%. (a) and (c) show model calculations compared to experiment results, (b) and (d) show generalized model calculations compared to experiment results.

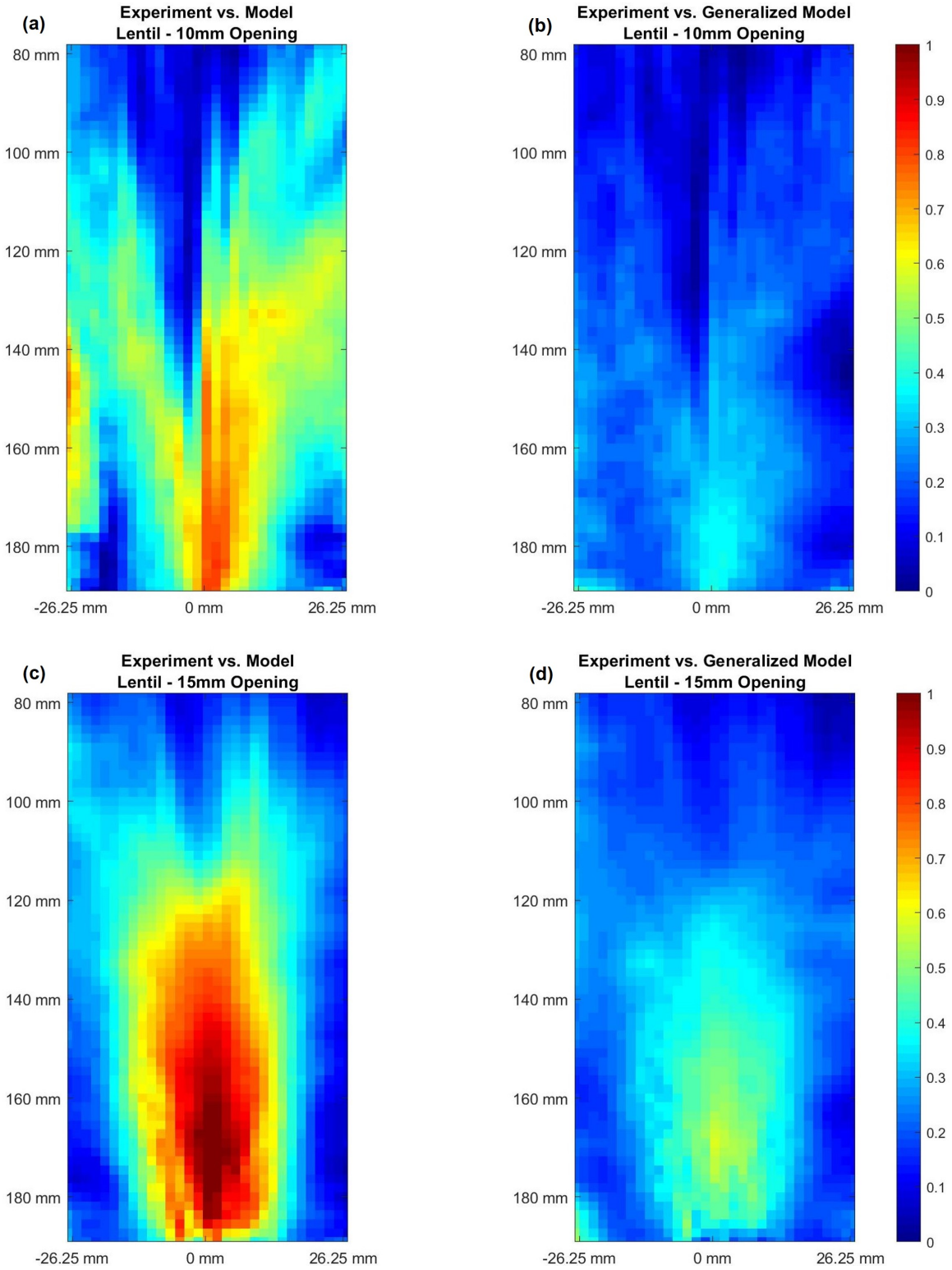


Figure 4.7: Difference percentage of the experiment, model and generalized model results of the orientational domain of Lentil discharge through 10mm and 15mm openings. The color bars provided for all four figures are showing the difference ranges between the orientational domains between 0% and 100%. (a) and (c) show model calculations compared to experiment results, (b) and (d) show generalized model calculations compared to experiment results.

the model and generalized model results compared to the experiment for both rice and lentil discharges through 10mm and 15mm openings, respectively. The color bars represent the percentage of the differences in each point. It can be seen that the generalized model can predict the orientational flow for both the middle and boundaries better than the model. Also, it can be observed that the generalized model results are in a better agreement with the experimental results in capturing the flow orientation near the openings of the hopper compared to the model.

From the results provided in Table (4.3) and Figures (4.6) and (4.7), it can be concluded that the generalized model is more advance in predicting the orientational flow of the grains compared to the kinematic model provided in [21]. Therefore, considering all provided results leads to the conclusion that the generalized model by carrying $\zeta$ as one of the components of model parameters establishes a better agreement with the experimental measurements compared to the model.

# Chapter 5

# Conclusion and Future Works

This chapter provides a summary of this work and presents the main results. Furthermore, it denotes the main improvements of the study and presents recommendations for potential future works.

## 5.1 Summary

Granular material flow is a broad and complex research field that challenges scientists and researchers, especially when it comes to the fluid-like behaviour of granular matter as it has the grain orientation effect in its nature. Most of the granular material available in nature and industries carries an asphericity aspect in their shape. This shape extension adds complexity to the flow characteristics and leads to complicated behaviours. Nadler et al. in [21] proposed a kinematic model that can capture the evolution of the orientation of ellipsoidal grains. In this work, the kinematic model presented in [21] was first numerically solved for the hopper discharging application using the setups provided in [22]. Then the performance of the model was investigated and compared with the experimental results of [22]. The model results, including the orientation field and the principal angle domain, were addressed in Chapter (4).

The location and the orientation of the grains, at the highest layer of the hopper, were considered identical in the model simulation and experiment. The prediction of the model showed that reorientation of the grains starts farther upstream for both openings compared to the experiment. Moreover, the zones with lower velocities were not captured by the model. Also, the effect of the grain shapes was captured more by the model, as the angle domains showed that the grains were more aligned with respect to each other during the flow compared to the experiment. This means that the model was not able to effectively capture the misalignment of the grains due to the collision. The model was not capable of predicting the distribution of the grains while they flow down the hopper, similar to the experiment. As a result, this model is less effective in capturing the orientational flow of an inhomogeneous flow.

The proposed model in [21] consists of only two model parameters, $\psi$ and $\lambda$, that are used along with the model to capture the characteristics of the flow. In [21] the model parameters were assumed to depend only on the shape ratio of the grains. In this work, the model parameters were generalized and their performance was extended by adding $\zeta$, the ordering parameter, to their functions. The method of proposing the initial form of the model parameters was discussed in (3.21) based on the model equations of (2.15). For simplicity, the proposed model parameters were considered to be linear in $r_g$ and $\zeta$. The feasibility of the proposed models was investigated by curve fitting the various homogeneous values of $\lambda$, $\psi$, $\zeta$ and $r_g$ provided in [21]. Then, the parameters of the generalized model were determined by means of an optimization method. This method minimized the differences of principal angle and ordering parameter of each orientational tensor between experiment and model to find the parameters. Later, the proposed model was simulated in the hopper discharging application using the conditions provided in [22]. The results were visualized and compared with the experimental results and were discussed in the Chapter (4).

The generalized model showed a better agreement with the experimental results in predicting the orientational tensors. It was seen that the generalized model calculations were able to better capture the distribution of the grains compared to the model. Also, it was observed that the generalized model not only can capture the orientational flow of the grains near the openings but also it is capable of capturing the zones with lower velocities better than the model. Furthermore, the misalignment of the grains from the direction of flow due to inter-grain collisions were captured more in the generalized model compared to the model. The funnelling and bulk flows happening due to various opening sizes were vivid in the generalized model results compared to the model results. Finally, the differences between the orientational tensors of the experiment with the model and generalized model were quantified using an error function. The difference percentages were visualized for the studied grains and openings. Also, the work improvement percentages were given in Chapter (4). As a result of all of the work, it was concluded that the two generalized model parameters show a better agreement with experimental results on predicting the orientational tensors in an inhomogeneous flow.

In a nutshell, the study succeeds its main objective of proposing a generalized model that can predict the evolution of the grains alignment in an inhomogeneuos matter with various velocities and orientation during the flow. The proposed model's predictions agreed with the available experimental data, and it was able to capture all the flow features essential for projecting the flow orientation.

## 5.2 Future Work

In this work, two model parameters $\lambda$ and $\psi$ were proposed to improve the performance of the kinematic model available in [21]. For simplicity, the proposed model

parameters were considered to be linear in $\zeta$ and $r_g$. However, for future works, these two model parameters can be considered to be nonlinear in $\zeta$ and $r_g$. Also, other objective characteristics such as the rate of deformation and other extensions of the orientational tensors can be added as dependencies to the model parameters to improve the performance of the model. Furthermore, this work was performed only based on the lentil and rice discharge flows in a flat bottom hopper. Therefore, other types of grains in different applications and flow conditions will be required to further evaluate the model. This study proved the performance of the proposed model in a 2-D case. Hence it is suggested to test the model in 3-D problems for future investigations.

# Bibliography

[1] Pierre-Gilles de Gennes. *From Rice to Snow*. Springer Japan, Tokyo, 2008.

[2] Daniel Hestroffer, Paul Sánchez, Lydie Staron, A Campo Bagatin, Siegfried Eggl, Wolfgang Losert, Naomi Murdoch, Eric Opsomer, Fahrang Radjai, Derek C Richardson, et al. Small solar system bodies as granular media. *The Astronomy and Astrophysics Review*, 27(1):1–64, 2019.

[3] Jacques Duran. Sands, powders, and grains: An introduction to the physics of granular materials. 2012.

[4] Hans J Herrmann, J-P Hovi, and Stefan Luding. Physics of dry granular media. 350, 2013.

[5] Farhang Radjai, Jean-Noël Roux, and Ali Daouadji. Modeling granular materials: century-long research across scales. *Journal Of Engineering Mechanics*, 143(4):04017002, 2017.

[6] Heinrich M. Jaeger, Sidney R. Nagel, and Robert P. Behringer. Granular solids, liquids, and gases. *Rev. Mod. Phys.*, 68:1259–1273, Oct 1996.

[7] Christopher E. Brennen. *Granular Flows*. Cambridge University Press, 2005.

[8] YC Tai, JMNT Gray, K Hutter, and S Noelle. Flow of dense avalanches past obstructions. *Annals of Glaciology*, 32:281–284, 2001.

[9] Yoël Forterre and Olivier Pouliquen. Flows of dense granular media. *Annu. Rev. Fluid Mech.*, 40:1–24, 2008.

[10] R. M. Nedderman. *Statics and Kinematics of Granular Materials*. Cambridge University Press, 1992.

[11] Isaac Goldhirsch. Rapid granular flows. *Annual review of fluid mechanics*, 35(1):267–293, 2003.

[12] P. C. Johnson and R. Jackson. Frictional–collisional constitutive relations for granular materials, with application to plane shearing. *Journal of Fluid Mechanics*, 176:67–93, 1987.

[13] Junyao Tang and Robert P Behringer. Orientation, flow, and clogging in a two-dimensional hopper: Ellipses vs. disks. *EPL (Europhysics Letters)*, 114(3):34002, 2016.

[14] Emilien Azéma, Itthichai Preechawuttipong, and Farhang Radjai. Binary mixtures of disks and elongated particles: Texture and mechanical properties. *Physical Review E*, 94(4):042901, 2016.

[15] Tamás Börzsönyi, Ellák Somfai, Balázs Szabó, Sandra Wegner, Pascal Mier, Georg Rose, and Ralf Stannarius. Packing, alignment and flow of shape-anisotropic grains in a 3d silo experiment. *New Journal of Physics*, 18(9):093017, 2016.

[16] Sandra Wegner, Ralf Stannarius, Axel Boese, Georg Rose, Balazs Szabo, Ellak Somfai, and Tamás Börzsönyi. Effects of grain shape on packing and dilatancy of sheared granular materials. *Soft Matter*, 10(28):5157–5167, 2014.

[17] Hui Ping Goh, Paul Wan Sia Heng, and Celine Valeria Liew. Comparative evaluation of powder flow parameters with reference to particle size and shape. *International journal of pharmaceutics*, 547(1-2):133–141, 2018.

[18] Pooja Shenoy, Maxime Viau, Kristel Tammel, Fredrik Innings, John Fitzpatrick, and Lilia Ahrné. Effect of powder densities, particle size and shape on mixture quality of binary food powder mixtures. *Powder Technology*, 272:165–172, 2015.

[19] Ahmed Ashour, Sandra Wegner, Torsten Trittel, T Börzsönyi, and R Stannarius. Outflow and clogging of shape-anisotropic grains in hoppers with small apertures. *Soft Matter*, 13(2):402–414, 2017.

[20] Tamás Börzsönyi and Ralf Stannarius. Granular materials composed of shape-anisotropic grains. *Soft Matter*, 9(31):7401–7418, 2013.

[21] B Nadler, F Guillard, and I Einav. Kinematic model of transient shape-induced anisotropy in dense granular flow. *Physical review letters*, 120(19):198003, 2018.

[22] François Guillard, Benjy Marks, and Itai Einav. Dynamic x-ray radiography reveals particle size and shape orientation fields during granular flow. *Scientific reports*, 7(1):1–11, 2017.

[23] Junyao Tang and RP Behringer. How granular materials jam in a hopper. *Chaos: An Interdisciplinary Journal of Nonlinear Science*, 21(4):041107, 2011.

[24] Iker Zuriguel, Daniel Ricardo Parisi, Raúl Cruz Hidalgo, Celia Lozano, Alvaro Janda, Paula Alejandra Gago, Juan Pablo Peralta, Luis Miguel Ferrer, Luis Ariel Pugnaloni, Eric Clément, et al. Clogging transition of many-particle systems flowing through bottlenecks. *Scientific reports*, 4(1):1–8, 2014.

[25] A Janda, Diego Maza, A Garcimartín, E Kolb, J Lanuza, and E Clément. Unjamming a granular hopper by vibration. *EPL (Europhysics Letters)*, 87(2):24002, 2009.

[26] Cristian Mankoc, Angel Garcimartín, Iker Zuriguel, Diego Maza, and Luis A Pugnaloni. Role of vibrations in the jamming and unjamming of grains discharging from a silo. *Physical Review E*, 80(1):011309, 2009.

[27] Luke Fullard, Daniel J Holland, Petrik Galvosas, Clive Davies, Pierre-Yves Lagrée, and Stéphane Popinet. Quantifying silo flow using mri velocimetry for testing granular flow models. *Physical Review Fluids*, 4(7):074302, 2019.

[28] Toshihiro Kawaguchi. Mri measurement of granular flows and fluid-particle flows. *Advanced Powder Technology*, 21(3):235–241, 2010.

[29] Stephen A Hall, Michel Bornert, Jacques Desrues, Yannick Pannier, Nicolas Lenoir, Gioacchino Viggiani, and Pierre Bésuelle. Discrete and continuum analysis of localised deformation in sand using x-ray $\mu$ct and volumetric digital image correlation. *Géotechnique*, 60(5):315–322, 2010.

[30] Krzysztof Grudzień, Maciej Niedostatkiewicz, J Adrien, J Tejchman, and E Maire. Quantitative estimation of volume changes of granular materials during silo flow using x-ray tomography. *Chemical Engineering and Processing: Process Intensification*, 50(1):59–67, 2011.

[31] Stephen A Hall, David Muir Wood, Erdin Ibraim, and Gioacchino Viggiani. Localised deformation patterning in 2d granular materials revealed by digital image correlation. *Granular matter*, 12(1):1–14, 2010.

[32] Thierry Faug, Philippa Childs, Edward Wyburn, and Itai Einav. Standing jumps in shallow granular flows down smooth inclines. *Physics of Fluids*, 27(7):073304, 2015.